ANNALS OF GEOPHYSICS, 67,1, PA108; 2024; doi:10.4401/ag-9016
OPEN ACCESS

Scintillation Climatology from a Software-Defined Radio Receiver over Antarctica

Rayan Imam[*,1], Lucilla Alfonsi[1], Luca Spogli[1,2], Claudio Cesaroni[1], Iman Ebrahimi Mehr[3], Alex Minetto[3], Fabio Dovis[3]

(1) Upper Atmosphere Physics and Radiopropagation Unit, Istituto Nazionale di Geofisica e Vulcanologia, Rome, Italy
(2) SpacEarth Technology, Rome, Italy
(3) Department of Electronics and Telecommunications, Politecnico di Torino, 10129 Torino, Italy

Article history: received September 28, 2023; accepted March 8, 2024

Abstract

Software-Defined Radio (SDR) Global Navigation Satellite System (GNSS) receivers for operational Ionospheric Scintillation Monitoring (ISM) have faced challenges and were deemed failures by many research projects. The need for a highly stable oscillator and a robust real-time signal-tracking capability have been the main challenges.

The Istituto Nazionale di Geofisica e Vulcanologia (INGV) led a project called DemoGRAPE (Demonstrator of GNSS Research and Application for Polar Environment) to deploy an SDR GNSS Receiver at SANAE IV Antarctica station, which has been continuously operating since January 2016. The SDR receiver was designed by the Navigation Signal Analysis and Simulation (NavSAS) group in collaboration with the Joint Research Centre (JRC) of the European Commission. The system deploys the SDR in parallel to a Septentrio PolaRxS ISM receiver. The two receivers are fed by the same receiving antenna (i.e., they share the same field of view and, hence, cross the same portion of the ionosphere) such that they receive quasi-identical signals except for the independent effects of their front-ends. The SDR produces as output a log file, equivalent to the ISM record produced by PolaRxS, that contains the amplitude and phase scintillation indexes. In addition to this, the SDR system records the raw digital samples of the GNSS signal when the internal algorithm of the receiver detects scintillation presence. These data can be used to replicate the scintillation event in the laboratory and perform dedicated post-processing of the raw signal itself.

The system has been in operation for over seven years now, spanning more than half a solar cycle. It has recorded several geomagnetic storm events as well as abundant data in quiet conditions. To the best of our knowledge, this is the longest dataset of this nature (co-located PolaRxS and SDR receivers). We compare the performance of the two receivers by analyzing the scintillation climatology maps obtainable from both receivers' data. Here, the climatology is obtained using the well-established Ground-Based Scintillation Climatology (GBSC) technique from the data provided by the two different receivers.

The study shows that the SDR climatology maps under disturbed geomagnetic conditions are equivalent to those obtained from the PolaRxS receiver. Under quiet conditions, the SDR shows more scintillation events than the PolaRxS. Carefully inspecting the differences in the scintillation occurrence between the two receivers, they seem not to happen randomly but mainly concentrated along the expected (climatological) position of the auroral oval. This means that the SDR application for space weather monitoring could be possible and that the SDR could be utilizable as an informative tool by the ionospheric scintillation community.

Keywords: GNSS; SDR; Ionospheric irregularities; Scintillation; High-latitude ionosphere; Polar areas

1. Introduction

The utilization of Global Navigation Satellite System (GNSS) signals as tools for monitoring the ionosphere has gained significant popularity. This is primarily due to the widespread availability of GNSS signals across the globe and the open access to most of these signals. In general, there are two approaches to ionospheric monitoring, especially when aiming at detecting ionospheric irregularities threatening GNSS signals (e.g., ionospheric scintillations). The first approach involves using commercial receivers, such as Ionospheric Scintillation Monitoring (ISM) Receivers (ISMRs) [see, e.g., Bougard et al., 2011; Van Dierendonck et al., 1993]. The second approach entails developing a monitoring station based on the Software-Defined Radio (SDR) paradigm [Dovis et al., 2004; Fernández-Prades et al., 2011; Presti et al., 2014]. Indeed, using commercial receivers has its limitations, with a major drawback being their closed-source nature and limited customization. These receivers are usually tailored for specific applications, which can constrain the ability to adjust or enhance algorithms, particularly those related to acquisition and tracking loops. This lack of adaptability can pose challenges when attempting to meet custom requirements or address specialized research objectives. For example, using a custom SDR receiver, [Pica et al., 2023] addressed the presence of particular types of Radio Frequency Interference (RFI) that were wrongly classified by commercial ISM receivers as scintillation events. Another illustrative case of specialized objective can be found in [Fernandez et al., 2020], which delves into how ionospheric scintillation affects the transmission of signals from a constellation of Low Earth Orbit (LEO) satellites using SDR technology. Furthermore, the cost and hardware limitations associated with commercial off-the-shelf ISM receivers can also be significant challenges.

The abovementioned limitations highlight the advantages of opting for SDR solutions. SDR is a radio communication system where software replaces many traditional hardware functions [Ulversoy, 2010]. It allows for flexible and programmable radio systems, making it possible to tweak the signal processing chain from the physical to the application layer through software rather than poorly-customizable hardware components. Therefore, SDRs are highly flexible and can quickly adapt to developing or modifying wireless communication architectures simply by changing software to support new communication services or protocols. Given its high flexibility, observing scintillation phenomena utilizing the SDR architecture has become more popular. The use of SDR offers several advantages, with signal recording being a primary benefit. For instance, in high latitudes regions, scintillations may occur at any time. Recording signals that have encountered these phenomena can be invaluable for subsequent analysis and research purposes. Moreover, noteworthy events are often monitored from stations situated in remote or hard-to-reach areas. In such cases, modifying high-end receivers' parameters may be challenging or impossible, while SDRs can be remotely controlled and monitored, allowing for remote maintenance and adjustments, even in inaccessible locations. Due to the configurability of SDR, receiver settings, including front-end parameters and the acquisition and tracking architecture, can also be altered. Additionally, this architecture provides access to intermediate and low-level signal processing stages, offering a more extensive range of observables in monitoring systems. This accessibility allows for integrating various GNSS software receivers within the same hardware framework. Additional advantages of SDR architecture have been detailed in the recent literature [Cristodaro et al., 2018; Cristodaro et al., 2018; Linty et al., 2016; Mehr et al., 2023; Pica et al., 2023; Imam et al., 2023].

Indeed, SDR architecture does have some disadvantages. One notable drawback is that SDRs can face difficulties with real-time processing, especially when dealing with very high sampling frequencies or extremely wide bandwidths. This challenge can lead to problems in transferring data between the front end and the processor, potentially resulting in issues such as sampling loss and the integrity of the recorded samples. Furthermore, the complexity of the system can be significantly higher, demanding expertise in both software and hardware to design, implement, and maintain effectively. Moreover, the power consumption of the entire system can be considerably greater compared to commercial receivers, as each component within the SDR architecture requires its own power source, potentially resulting in increased overall power consumption.

SDR technology has been present in ionospheric scintillation data collection campaigns as a tool for recording and offline processing GNSS signals [Curran et al., 2015; Linty et al., 2015; Morton et al., 2014), and many researchers have demonstrated its ability to track the GNSS signals under strong scintillation conditions [Linty et al., 2018]. In this work, we focus on scintillation climatology, by processing a four-year dataset from a continuously running GNSS SDR receiver that was developed to demonstrate the operational capabilities of this technology. To our knowledge, this is the very first attempt to derive scintillation climatology from an SDR receiver, with a particular focus on high latitude.

In late 2015, the Demonstrator of GNSS Research and Application for Polar Environment (DemoGRAPE) project installed a prototype GNSS SDR system in the South African base SANAE IV station (71°40′22″S, 2°50′26″W, geomagnetic dipole latitude 66°45′S). The international project was funded by the Italian National Program for Antarctic Research and led by the Istituto Nazionale di Geofisica e Vulcanologia, in collaboration with Politecnico di Torino, LINKS Foundation (former Istituto Superiore Mario Boella), the South African National Space Agency and the Brazilian National Institute of Space Physics. The SDR shares the antenna and works in parallel with a commercial Septentrio PolaRxS ionospheric monitoring receiver, and both systems have been monitoring the ionosphere continuously since installation [Alfonsi et al., 2016].

The receivers have been fully operational since January 2016, covering the decaying phase of solar cycle 24 (2016-2018), the quiet phase of the same solar cycle (2019-2021), and the ascending phase of solar cycle 25 (2022-now) that is expected to peak in the period 2025-2027. To show the geomagnetic conditions during the considered time window, Figure 1 (a) and (c) show the time series for the 1-hr Dst (Disturbance storm time) and 3-hr planetary Kp indexes [Kauristie et al., 2017], respectively, from January 2016 to December 2022. The figure also shows in panels (b) and (d) the histograms of the Dst and Kp indexes on logarithmic scales, respectively, highlighting the number of times each index range occurred. The Kp index monitors on a global scale the sub-auroral geomagnetic disturbance. Kp above four is considered disturbed geomagnetic conditions, with the storm strength increasing from minor to moderate to major as Kp increases from 5 to 9. Kp above 6 and Dst. below −100 nT are considered major geomagnetic storms [Zhang et al., 2007].

In this paper, we analyze the period 2016-2019, which is under low solar activity conditions. Notably, even under these generally quiet geomagnetic conditions, some significant geomagnetic storms occurred, inducing scintillation events in the high-latitude regions, like the one that occurred in September 2017 [D'Angelo et al., 2021; Linty et al., 2018; Spogli et al., 2021]. It is well known that scintillation may occur at any time, including under quiet geomagnetic conditions. It is also known that under disturbed geomagnetic conditions scintillation may not arise [De Franceschi et al., 2008]. Taking this in mind, throughout this article, we will be referring to "quiet" and "disturbed" as related to geomagnetic conditions. The four-year dataset is long enough to drive scintillation climatology maps for quiet conditions and verify it against literature covering the same and previous solar cycles. Moreover, the number of geomagnetic events that induced the formation of ionospheric irregularities in the high latitudes is large enough to conduct an initial assessment of the receiver capabilities under disturbed conditions in preparation for the expected solar cycle peak in 2025.

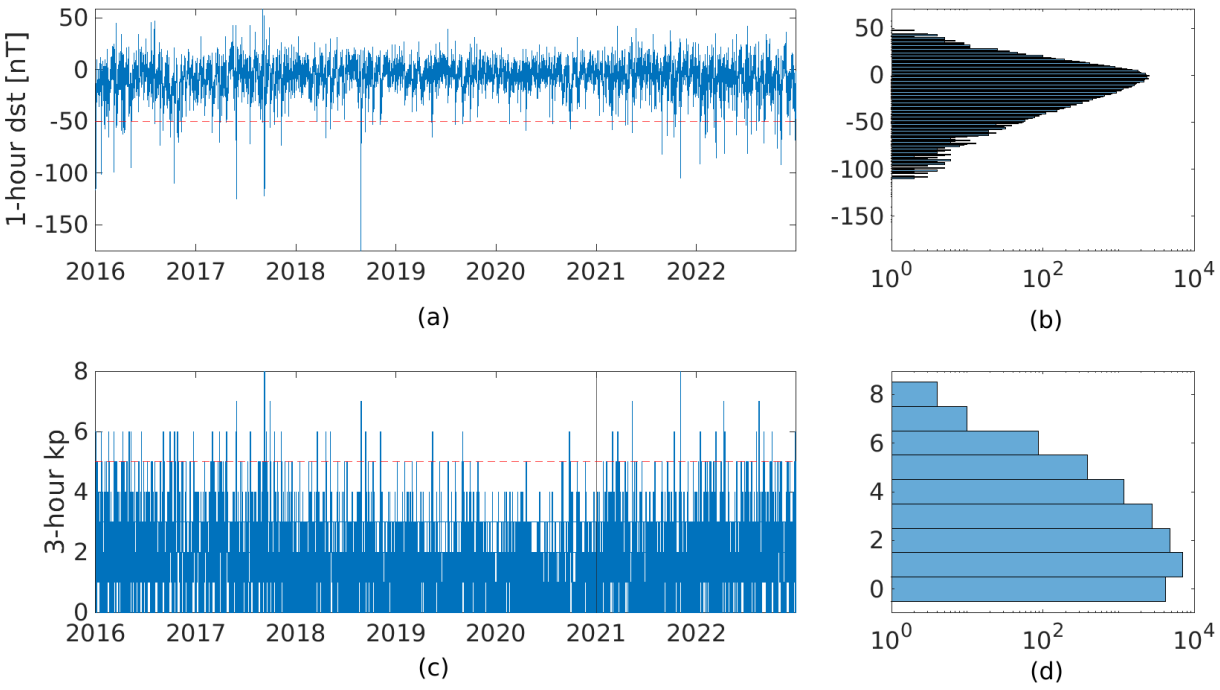

Figure 1. (a) Dst and (c) Kp indexes 2016-2022 and histogram of the number of events in each (b) Dst and (d) Kp index range.

The fact that the SDR is installed in parallel to the widely used Septentrio PolaRxS commercial ISM receiver [Bougard et al., 2011] adds a unique dimension to this comparison. For this comparison, we chose to use synchronous SDR-PolaRxS datasets. This means that the dataset includes only the instances where the two receivers were simultaneously successfully tracking (to be precise, simultaneously giving measurements for) a GNSS signal. This implicitly implies that this comparison does not emphasize the performances of the receivers in terms of signal tracking and processing capabilities under challenging ionospheric conditions that may lead to tracking loss, which deserves independent analyses worth a further article. However, this article includes an assessment of the difference between the two receivers in estimating the amplitude and phase scintillation indexes.

The article is organized as follows. Section II describes the scintillation monitoring stations at SANAE, covers the computation of the scintillation indexes from GNSS receivers' measurements, and introduces the Ground-Based Scintillation Climatology technique. Section III describes the experimental datasets and the methodology. Section VI is dedicated to the results and discussion. The conclusions are derived in Section V.

2. Background

2.1 Monitoring station architecture

As discussed in the previous section, one of the most intriguing ways to pursue monitoring of ionospheric scintillation is by applying SDR techniques. These techniques not only facilitate the real-time recording and processing of signal samples, but also enable subsequent post-processing for more comprehensive analysis. Generally, within the system architecture built upon SDR, a front-end is equipped to capture signals with enhanced resolution. The front end typically consists of the hardware components responsible for receiving the Radio Frequency (RF) signal from the antenna and converting signals into digital data samples that the rest of the systems can process. The GNSS monitoring architecture employed in this context is illustrated in Figure 2 [adapted from Alfonsi et al., 2016], and a more detailed explanation of each component is provided subsequently.

1) GNSS antenna: is a multi-band antenna capable of supporting multiple satellite constellations, including GPS, GLONASS, and Galileo.
2) Mini-circuits RF splitter: It is employed to split the received signal at the antenna and distribute the RF signal to both the GNSS ISMR receiver and the RF front-ends.
3) Low Noise Amplifier (LNA): It's a line amplifier equipped with a DC filter designed to amplify the GNSS signals.

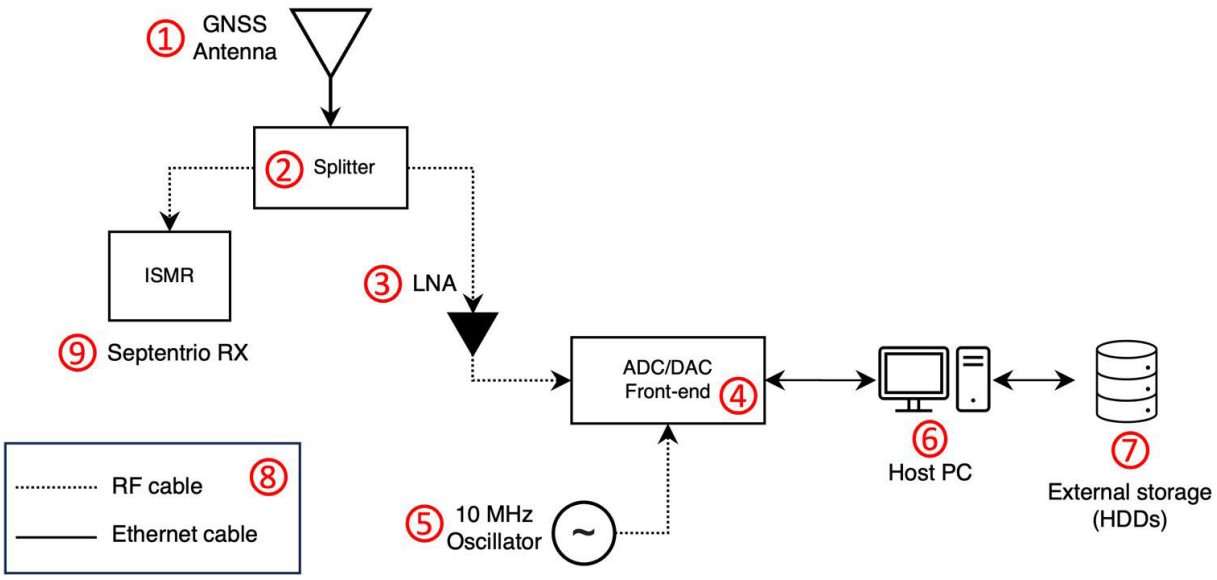

Figure 2. The architecture of the scintillation monitoring system installed at SANAE IV station

4) Front-end: The front-end equipment utilized comprises Universal Software Radio Peripheral (USRP) N210 devices, responsible for conducting the ADC conversion of the input signal and delivering a stream of Intermediate-Frequency (IF) In-Phase/Quadrature (I/Q) data.
5) Rubidium atomic clock: It furnishes a reliable and stable clock reference for the USRP's front-end, in particular to its ADC.
6) Host PC: It is responsible for executing the routine program that manages the stream of digitized signals and stores them. Additionally, the fully software GNSS receiver operates on the PC computer.
7) External-storage: Since the disk capacity for storing raw samples in host-pc is limited, the recorded raw will be transmitted to the external storage. As an example, recording I/Q samples of a GNSS signal at an IF with a sampling frequency of 5 MHz for a duration of 50 minutes, the resulting data size would be approximately 30 gigabytes (GB).
8) Cabling: The front-end has the capability to communicate with the host PC through Ethernet, and both of them are connected to a router, where the computer is also connected.
9) ISMR: The receiver used for this context is the Septentrio PolaRxS, a specialized receiver employed to monitor and investigate ionospheric scintillation phenomena.

At the software architecture level, a complete GNSS software receiver is utilized to extract the scintillation indexes. This software receiver is known as 4tuNe and was developed by the Joint Research Centre (JRC) of the European Commission (EC). It features a modular and reconfigurable architecture, allowing it to perform scintillation monitoring functions that are on par with those carried out by commercial solutions [Curran et al., 2014].

2.2 GNSS Scintillation Indexes

The amplitude scintillation index (S4) is the standard deviation of the detrended received signal intensity (SI) normalized to the average signal intensity [Briggs & Parkin, 1963]. This S4 definition applies to any trans-ionospheric communication signal, transmitted by any satellite at any orbit above the ionosphere. S4 over the observation window T_w is given by [Fremouw et al., 1978]:

$$S4 = \sqrt{\frac{\langle SI^2 \rangle - \langle SI \rangle^2}{\langle SI \rangle^2}}, \tag{1}$$

where $\langle . \rangle$ is the average over T_w and SI is the detrended signal intensity. S4 corresponds then to the amplitude scintillation index of the previous time window.

When applied to GNSS-based scintillation monitoring, the terms detrending and signal intensity are not trivial. The signal intensity estimated by a GNSS receiver is affected by receiver-dependent noise and gain. These can be removed by subtracting the noise contribution (typically estimated by the receiver) and normalizing the signal intensity. Scintillation monitoring receivers choose to counter the noise in various ways. Some receivers eliminate the receiver noise before applying the detrending filter [Crowley et al., 2011]. Other receivers choose to remove the receiver noise by subtracting the predicted S4 due to the noise factor from the standard deviation in SI, for example [Van Dierendonck et al., 1993). Some receivers implement neither. The most common method to calculate S4 from GNSS measurements taking into account the effect of the ambient noise, if not already removed from SI, is [Van Dierendonck et al., 1993]:

$$S4_{after\ noise\ correction} = \sqrt{\frac{\langle SI^2 \rangle - \langle SI \rangle^2}{\langle SI \rangle^2} - \frac{100}{C/N_0}\left[1 + \frac{500}{19\ C/N_0}\right]}, \tag{2}$$

where C/N_0 is the carrier-to-noise ratio estimated by the receiver, and the overall term $\frac{100}{C/N_0}\left[1 + \frac{500}{19\ C/N_0}\right]$ corresponds to the tracking-loop phase noise variance [Holmes, 1982; Portella et al., 2021].

The signal intensity is also affected by the propagation losses that are induced by factors other than the irregularities in the ionosphere. Detrending aims to remove the latter effects. When detrending the signal intensity,

a low-pass version of SI is subtracted from SI to remove the non-scintillation-related components. The filter applied is usually a sixth-order Butterworth low pass filter with 0.1 Hz cutoff frequency [Rino et al., 1981; Van Dierendonck et al., 1993], but other detrending methods are also present in the literature. For example, [Van Dierendonck & Arbesser-Rastburg, 2004] exploit the wide and narrow band power, WBP and NBP respectively, to detrend the signal. NBP, WBP and the detrended signal intensity as:

$$WBP = \Sigma_{m=1}^{M}(I_m^2 + Q_m^2), \tag{3}$$

$$NBP = \Sigma_{m=1}^{M} I_m^2 + \Sigma_{m=1}^{M} Q_m^2, \tag{4}$$

$$SI = \frac{NBP - WBP}{\langle NBP - WBP \rangle}, \tag{5}$$

where M is the number of samples in the integration window (20 ms is common for GPS L1/CA signals and for Galileo) and $\langle . \rangle$ is the average over T_w. Filtering techniques, other than the sixth-order Butterworth filter, claim to give a better estimation of S4 [Materassi & Mitchell, 2007; Najmafshar & Skone, 2014], and thus S4 estimation changes with the detrending method in use [Materassi et al., 2009; Najmafshar & Skone, 2014].

The phase scintillation index σ_ϕ is defined as the variance of the detrended phase. It is computed from:

$$\sigma_\phi^2 = \int_{f_c}^{\infty} P_\phi(f) df \approx \frac{2T}{(p-1) f_c^{p-1}} = \langle \phi^2 \rangle - \langle \phi \rangle^2, \tag{6}$$

where f_c is the lowest frequency admissible by the system, P_ϕ is the phase spectrum, P is the phase spectral power, P is the spectral index, ϕ is the raw phase, and $\langle . \rangle$ is the detrending operation.

This detrending and f_c have been a topic of debate among the scientific community for a long time, especially for high-latitude scintillations [Forte, 2005; Forte & Radicella, 2002; Ghobadi, Spogli, et al., 2020; McCaffrey & Jayachandran, 2019; Spogli et al., 2022; Wang et al., 2018]. Such recent literature highlights how the differences in the meaning of scintillation, and the perils of using the phase scintillation index retrieved with fixed cut-off frequency, that may lead to a wrong estimation of the relative balance between refractive (deterministic) and diffractive (stochastic) effects in the found patterns of scintillation indexes. These late findings suggest that scintillation is only due to stochastics effects, which are the most threatening for GNSS, and that they cannot simply be removed by combinations of GNSS observables. On the other hand, refractive effects, causing the bulk of the phase scintillation index fluctuations in the high-latitude sector, can be removed by using combinations like the ionosphere-free linear combination and they are suggested to be called simply as “phase fluctuations”. Diffractive effects affect signal amplitude and phase. They are due to irregularities that are below the Fresnel’s scale for L-band and GNSS observational geometry, i.e. of the order of few hundreds of meters. Refraction affects only the phase of the signal, and it is due to all ranges of scales, being the meso-scale (from km to few tens of km) the one mostly involved.

Bearing this in mind, we let the reader notice that ISM receivers implement phase detrending in various ways. For example, the receiver in [Crowley et al., 2011] implements a polynomial fit to remove the high-frequency noise and uses a third-order polynomial subtraction to filter out the low-frequency phase variations. Then, it applies Eq. (6) on a 100 s cadence to estimate σ_ϕ. However, the most common way to detrend ϕ uses a sixth-order high-pass digital Butterworth filter with 0.1 Hz cutoff frequency, then estimates σ_ϕ from Eq. (6) on a 60s cadence.

A comparison of the calculated scintillation indexes by a selection of ISM receivers can be found in de Paula et al. [2021] and in Ghobadi et al. [2020]. Here, we just highlight that i) estimating the noise-free signal intensity and the detrending operation are not trivial, ii) the type of receiver in use controls how the indexes were calculated, and iii) since we are comparing two receivers the indexes estimated will be different to some degree. The PolaRxS has a firmware that implements the calculation of the scintillation indexes while the SDR has a software routine that calculates the indexes using Eq. (1) and Eq. (3).

An early comparison that shows a good correlation between the indexes estimated by PolaRxS and the SDR at SANAE IV can be found in [Alfonsi et al., 2016]. Figure 3 shows an example of the indexes estimated by the two

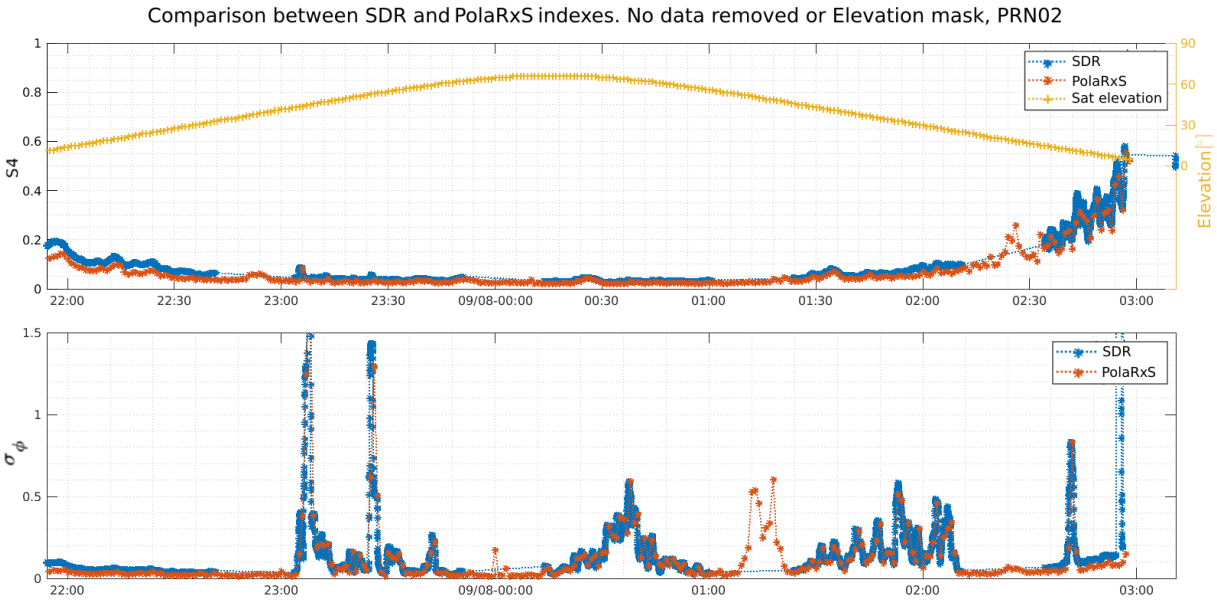

Figure 3. Time series of S4 (top) and σ_ϕ (bottom) for PRN02 between 22:00 and 03:00 UTC 7-8 September, estimated by the SDR (blue) and PolaRxS (red). The right y-axis of the top panel shows the elevation of the GNSS satellite (yellow).

receivers reporting mainly strong phase fluctuations due to meso-scale irregularities and increased values of the S4 index for low-elevation angles, mostly due to multipath effects. For this demonstration, we choose the September 2017 event, which was one of the strongest geomagnetic storms of solar cycle 24. The figure shows the time series of S4 (top) and σ_ϕ (bottom) for PRN02 between 22:00 and 03:00 UTC 7-8 September, estimated by the SDR (blue) and PolaRxS (red). The right y-axis of the top panel shows the elevation of the GNSS satellite (yellow). The 5-hour data starts as the satellite rises in the horizon until it is out of the field of view of the antenna. The PolaRxS continuously monitors the signal, while the SDR data consists of 50 minutes of data followed by approximately 20 minutes of data gap due to the configuration of the receiver for grabbing and processing the signal.

The figure highlights the two receivers' ability to track the signals under strong scintillation. Looking at the top panel, the two receivers' indexes are almost identical, even when the signal started to show multipath signatures around 02:30 UTC when the satellite elevation was ~10°. The same is true for σ_ϕ, except when the SDR starts to lose the signal as the satellite is exiting the field of view of the antenna, where the SDR gives infinite values to the σ_ϕ index. Other than that, the SDR was able to estimate the index with performance similar to PolaRxS.

2.3 Ground-Based Scintillation Climatology

Measurements of ionospheric scintillation have been continuously collected since the first artificial satellites in the 1950s, and the preceding radio star measurements in the 1940s [Chie Yeh & Liu, 1982]. To interpret these measurements, many theories of radio wave scattering have been applied [Yeh & Liu, 1982; Priyadarshi, 2015] and various ionospheric scintillation models have been developed [Béniguel, 2002; Secan et al., 1997; Wernik et al., 2007]. A recent review that covers the climatology of ionospheric scintillation over polar regions can be found in [Alfonsi et al., 2022].

Ground-Based Scintillation Climatology (GBSC) map is a well-established technique for identifying the areas of the ionosphere where scintillation is likely to occur [Alfonsi et al., 2011; De Franceschi et al., 2019; Spogli et al., 2009]. GBSC relies on constructing maps of the percentage of occurrence of the scintillation indexes in Altitude Adjusted Corrected Geomagnetic Coordinates [Baker & Wing, 1989; Shepherd, 2014], i.e. Magnetic Latitude (MLAT) vs. Magnetic Local Time (MLT). Throughout this paper, the percentage of occurrence is evaluated for each bin of 1° MLT (i.e. 4 minutes) ×1° MLAT as:

$$occ = \frac{N(\alpha > \beta)}{Ntot} \tag{7}$$

where $N(\alpha > \beta)$ is the number of instances where the index α is above a certain threshold β and $Ntot$ is the total number of data points inside that bin.

The auroral oval boundaries given by the Feldstein, Holzworth and Meng model for quiet (IQ = 0) and disturbed (IQ = 6) magnetic activity levels are superimposed on all the maps in this paper to indicate the approximate position of the oval and its displacement due to Geospace forcing. Scintillation occurrence is indeed expected to be observed inside and at the edges of the auroral ovals where electron density irregularities are more likely to occur. It is important to mention here that i) the Feldstein oval underestimates strong disturbance conditions [Spogli et al., 2009], and ii) the description of the oval is climatological, which suits the objective of this article.

In this paper, the GBSC maps will be displayed in polar maps, with the longitudes representing MLT and the latitudes representing MLATs. The centre of the plot is 90° magnetic South, 00:00 MLT is shown at 180° longitude line, and MLT is increasing anti-clockwise.

3. Methodology

3.1 Data availability

From the ISM receiver, 1450 days of data are available in the period 2016-2019 with only 11 days of data that are completely missing. From the SDR, 1437 days of data are available with 24 days of data completely missing between 2016-2019. The dataset used in this study contains the synchronized ISM and SDR receivers' data and is composed of 1426 days of data out of 1461 days. The synchronization assures that both receivers' data are available from the same satellite accepting a maximum ±0.5 second shift between the two receivers' measurements. Indeed, the SDR was working on the 11 days that PolaRxS was not working, acting as a backup ISM receiver.

All the PolaRxS scintillation and Total Electron Content (TEC) data are downloadable from the eSWua website www.eswua.ingv.it [Upper atmosphere physics and radiopropagation Working Group, 2020]. The SDR data are owned by NavSAS and INGV and are not available on the eSWua portal yet.

3.2 The receiver field of view

The location of SANAE IV, shown in Figure 4, describes how the station can observe ionospheric scintillations from inside the polar cap under strong geomagnetic storms to sub-auroral regions in quiet conditions. Panel (a)-(d) of Figure 4 show the Antarctic auroral oval as predicted by the Feldstein, Holzworth and Meng model [Feldshteyn, 1963; Holzworth & Meng, 1975] at 00:00, 06:00, 12:00 and 18:00 MLT, respectively. The oval between the two solid black circles indicates the oval when the disturbance level is weak (magnetic activity index IQ = 0) and will be referred to as IQ0 OA, while the one between the two red circles indicates the oval under strong disturbance (IQ = 6) and will be referred to as IQ6 AO. The figure also shows an approximation of the field of view of the GNSS antenna with two elevation mask angles, represented by dashed red lines for 30° and dashed black lines for 0°. Therefore, when the auroral oval overlaps with this dotted circle, scintillations and phase fluctuations could be observed by the receiver [De Franceschi et al., 2019; Jin et al., 2016; Nishimura et al., 2023; Spogli et al., 2009]. But also inside the inner auroral boundary, the polar cap can host scintillations [De Franceschi et al., 2008; Hong et al., 2020; Moen et al., 2013; Spogli et al., 2022]. Under disturbed conditions, a significant portion of the oval falls well within the field of view of SANAE station, especially if the elevation mask is lowered to 0°.

3.3 Sidereal multipath removal

From a GNSS receiver point of view, Figure 4 indicates that the receiver is observing scintillations mainly at low elevations (i.e., in the horizon) towards the polar cap. However, low-elevation data are usually removed by the elevation mask that is generally applied for multipath avoidance. Such a mask will remove a considerable part of the significant scintillation data. For this reason, we alternatively implemented a sidereal multipath mask instead of the elevation mask [McCaffrey and Jayachandran, 2017]. Since the multipath sources around the antenna at SANAE IV do not vary frequently, it is safe to assume that the multipath source is static for 7 days. We thus took the average

S4 value for 7 days, 3 days before and after the measurement day, each day shifted by 4 minutes w.r.t the previous one, as an estimation of the sidereal S4 value. The sidereal repeated S4 inflations are indicators of static multipath sources and not scintillations. The latter are random by nature, and we do not expect to see the same scintillation with sidereal repetition.

To complete the picture of the advantages of using the sidereal multipath mask instead of the elevation mask, we show in Figure 5 the number of binned samples, in magnetic (top) and geographic (bottom) coordinates (a) for all data, (b) after applying the sidereal multipath mask, (c) applying a 30° elevation mask, and (d) applying a 10° elevation mask. The bin size is 1°x1° (1° = 4 minutes MLT). The ionospheric piercing point is calculated at height of 350 km. For the bottom plots, we show the Feldstein auroral oval at 00:00 MLT, which highlights the best scenario for the receiver field of view inside the auroral ovals.

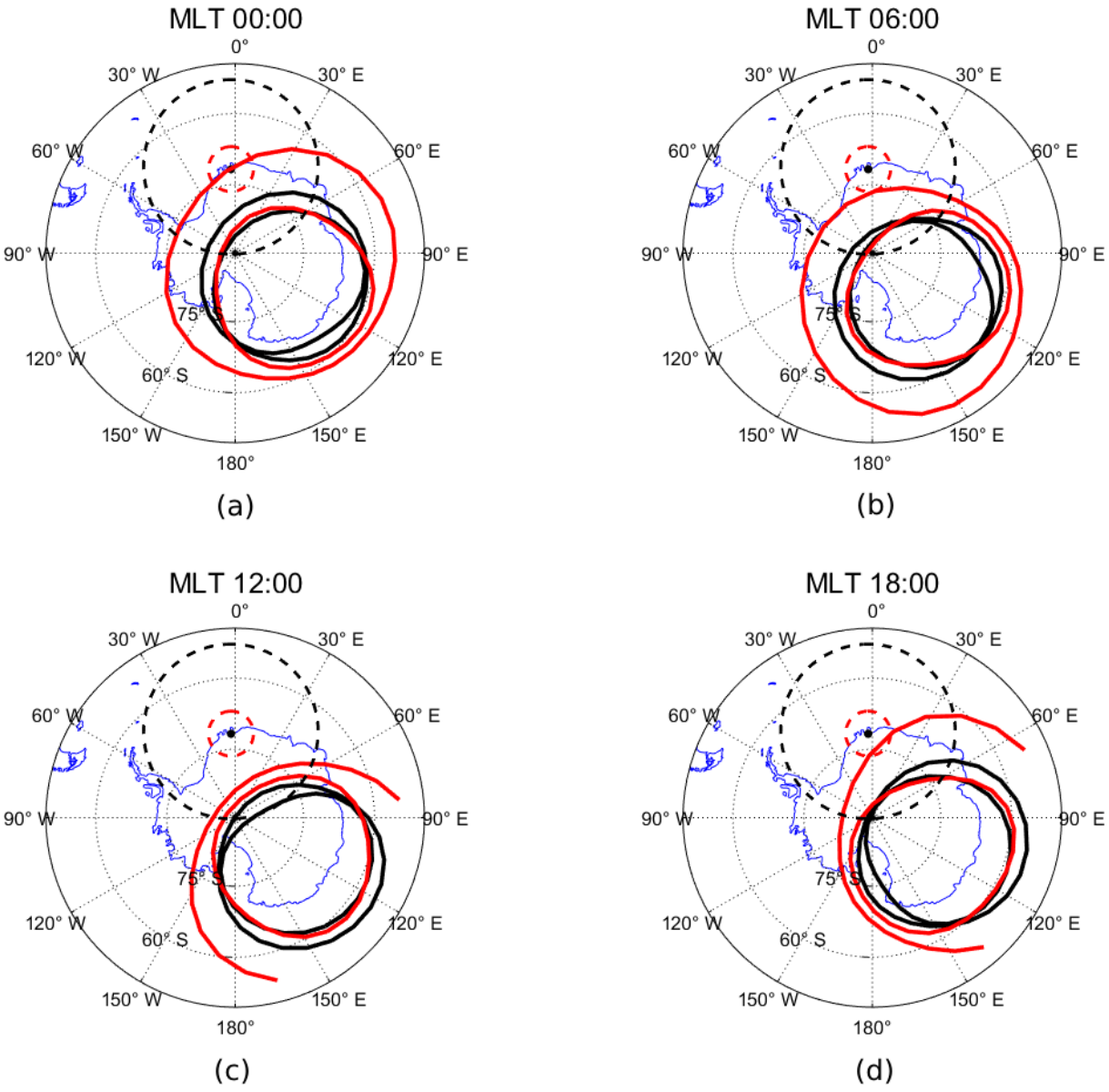

Figure 4 . The geographic and magnetic position of SANAE IV station with respect to the climatological Feldstein Auroral oval at (a) 00:00, (b) 06:00, (c) 12:00 and (d) 18:00 MLT. The oval between the two solid black circles indicates the oval when the disturbance level is weak (magnetic activity index IQ = 0), while the one between the two red circles indicates the oval under strong disturbance (IQ = 6). The approximate field of view of the GNSS receiver with 30° and 0° elevation mask angles is shown in dashed red and dashed black.

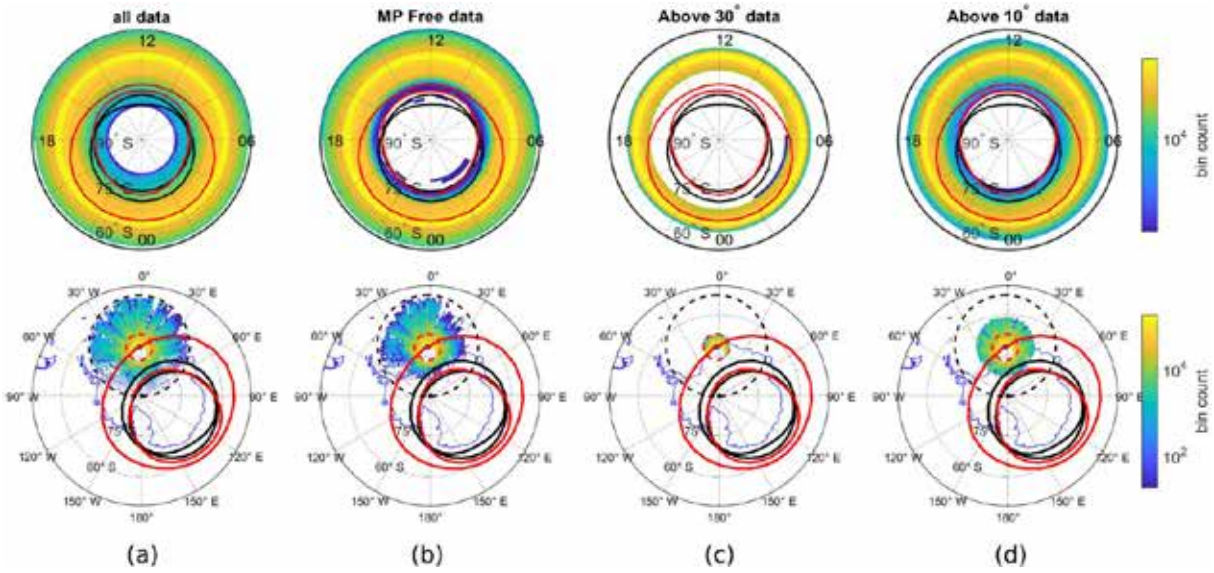

Figure 5. The histogram of SANAE IV data binned to 1° × 4 minutes magnetic MLAT,MLT (top) and 1°x1° geographic lat,lon (bottom) coordinates for (a) all the data, (b) sidereal multipath free data, (c) data above 30° elevation, and (d) data above 10° elevation. The Feldstein Auroral Oval corresponds to 00:00 MLT.

3.4 Scintillation climatology

In this paper, and referring to Eq. (7), $\alpha \in \{S4, \sigma_\phi\}$ and $\beta \in \{0.25, 0.5\}$. Similar scintillation strength thresholds were used in related publications [Pica et al., 2023]. To avoid including bins with poor statistics, bins with $Ntot$ less than 100 data points were discarded throughout the analysis, unless otherwise specified. Discarded data points take null values, and they appear on the maps as unavailable data with white colour. The GBSC maps for the following quantities were considered:

- For the SDR and PolaRxS separately, the occurrence of S4 > 0.25 (weak to moderate), S4 > 0.5 (moderate to strong), $\sigma_\phi > 0.25$ rad (weak to moderate), and $\sigma_\phi > 0.5$ rad (moderate to strong).
- From PolaRxS only, the mean and standard deviation of the Rate of TEC (ROT) in TEC unit (TECu) are reported per minute in each bin.

The absolute value of the difference between S4 and σ_ϕ given by the SDR and the PolaRxS, $S4_{diff}$ and $\sigma_{\phi\,diff}$ respectively, were calculated. The GBSC maps of the following quantities were generated:

- The occurrence of $S4_{diff} > 0.25$, $S4_{diff} > 0.5$, $\sigma_{\phi\,diff} > 0.25$ rad and $\sigma_{\phi\,diff} > 0.5$ rad.
- The mean and standard deviation of $S4_{diff}$ and the mean and standard deviation of $\sigma_{\phi\,diff}$ in each bin.

To facilitate a quantitative comparison of the accuracy of the SDR for various scintillation parameters $P \in \alpha$, climatological cases ($\alpha > \beta$), and geomagnetic conditions (quiet and disturbed), a single normalized percentage difference R_{diff} was derived using the following expression:

$$R_{diff} = \frac{\langle |P_{SDR} - P| \rangle}{\langle P \rangle} \cdot 100\% \quad \forall \quad P_{SDR} > \beta \tag{8}$$

where $\langle |P_{SDR} - P| \rangle$ is the mean absolute difference between SDR and PolaRxS for parameter $P \; \forall \; P \in \alpha$, for all the data points where P estimated by the SDR receiver (P_{SDR}) exceed a threshold value β, and $\langle P \rangle$ is the mean of corresponding values of parameter P estimated by Septentrio's receiver.

The overall dataset was split according to the Kp index (www.swpc.noaa.gov/noaa-scales-explanation) in two subsets:

- Data with Kp < 5 were utilized to construct the GBSC maps for quiet conditions, and
- Data with Kp ≥ 5 were utilized to construct the GBSC maps for disturbed conditions.

Furthermore, each subset was divided into two groups according to the SDR σ_ϕ ($\sigma_{\phi\ SDR}$) index:

- Group with $\sigma_{\phi\ SDR} \leq 2$ rad, indicating the data points where the SDR did not have peculiar signal phase measurements, and
- Group with $\sigma_{\phi\ SDR} > 2$ rad, indicating the data points where the SDR had peculiar signal phase measurements.

The SDR σ_ϕ threshold of 2 rad is a reasonable heuristic we established for the current analysis. The optimization and refinement of this quantity is beyond the scope of this article. We chose 2 rad because it is slightly above the σ_ϕ associated with extreme GNSS signals phase fluctuations recorded by the ISMR along the entire station campaign.

The sidereal multipath mask eliminates 15% of the dataset (compared to 51% that would have been eliminated by a 30° elevation mask). In total, approx. 16,000,000 samples were available for conducting the climatology maps. A sample is the set of measurements {SDR S4, ISMR S4, SDR σ_ϕ, ISMR σ_ϕ, ISMR ROT, $S4_{diff}$, $\sigma_{\phi\ diff}$} obtained from a satellite signal, provided at 1-minute cadence. Only the GPS constellation is considered in this study.

4. Results and discussion

4.1 SDR vs. PolaRxS scintillation climatology under quiet conditions

Figure 6 shows S4 and σ_ϕ climatology maps under quiet conditions from the SDR (top) and PolaRxS (bottom) for (a) S4 > 0.25 (b) S4 > 0.5 (d) $\sigma_\phi > 0.25$ rad and (e) $\sigma_\phi > 0.5$ rad, with bin size 1°x1°. The figure shows also (c) the mean (top) and standard deviation (bottom) of ROT, which is provided by PolaRxS multifrequency GNSS measurements.

We start by looking at the mean and standard deviation of ROT. Mean ROT in the morning/noon sector (09:00-16:00 MLT) at the lowest MLATs is significantly higher than the other sectors due to the photoionization process. The standard deviation of ROT takes its greatest values at the edge of the IQ0 and IQ6 AO, in the evening and night sectors. As shown in [Alfonsi et al., 2011] Table 3, high ROT and ROTrms (here ROT standard deviation) are indications of irregularities of all scales, which might include the small scale irregularities that induce GNSS amplitude and phase scintillations.

SDR S4 suggests S4 > 0.25 occurrence in the noon sector at low MLATs and S4 > 0.5 occurrence in the night sector exactly at the edge of the IQ0 AO and between 00:00-01:00 MLT at all MLATs. These observations are not visible for the PolaRxS receiver. SDR S4 > 0.5 and PolaRxS S4 > 0.25 however show similar occurrence percentages in the afternoon sector at all MLATs. PolaRxS did not observe S4 > 0.5 occurrence under quiet conditions.

σ_ϕ from the SDR receiver is peculiar as anticipated in Section II Figure 3. Nevertheless, since these peculiarities are random and equally distributed for all the MLAT and MLT, real phase fluctuations occurrence adds on top of the noisy climatological map. However, σ_ϕ occurrence under quiet conditions is in the range of 1% as shown in PolaRxS $\sigma_\phi > 0.25$ rad occurrence, which made the SDR σ_ϕ maps useless in this case. Nonetheless, $\sigma_\phi > 0.5$ rad from the PolaRxS shows the same occurrences revealed by the S4 > 0.5 from the SDR in the night sector. Finally, PolaRxS $\sigma_\phi > 0.5$ rad inside the IQ6 AO agrees with the map of ROT standard deviation.

Next, we take $\sigma_{\phi\ SDR}$ as an indicator for sorting the quiet conditions data into out of the dynamic range of the SDR tracking loops ($\sigma_{\phi\ SDR} > 2$ rad) and within the tracking capabilities of the SDR tracking loops ($\sigma_{\phi\ SDR} \leq 2$ rad).

Figure 7 shows the climatology maps of all the data where the SDR $\sigma_\phi \leq 2$ rad under quiet conditions. The maps of PolaRxS S4, σ_ϕ and ROT do not change while the maps of occurrence of S4 > 0.5 from the SDR are different w.r.t the general case (Figure 6). S4 > 0.5 occurrence in the afternoon sector disappeared while S4 > 0.5 occurrence at the edge of the IQ6 AO night sector is still visible.

Figure 8 shows the climatology of all the data where the SDR $\sigma_\phi > 2$ rad under quiet conditions. Such SDR σ_ϕ peculiarities are associated to SDR S4 > 0.5 at the outer edge of the IQ0 and IQ6 auroral ovals right after midnight. From the PolaRxS, only S4 > 0.25 at the low MLATs night sector is noticeable. PolaRxS σ_ϕ occurrence inside the IQ6 AO all night is evident, especially at the edge of the IQ0 AO around 3:00 MLT. In general, the PolaRxS $\sigma_\phi > 0.25$ rad map seems to partially agree with the SDR S4 > 0.5 map.

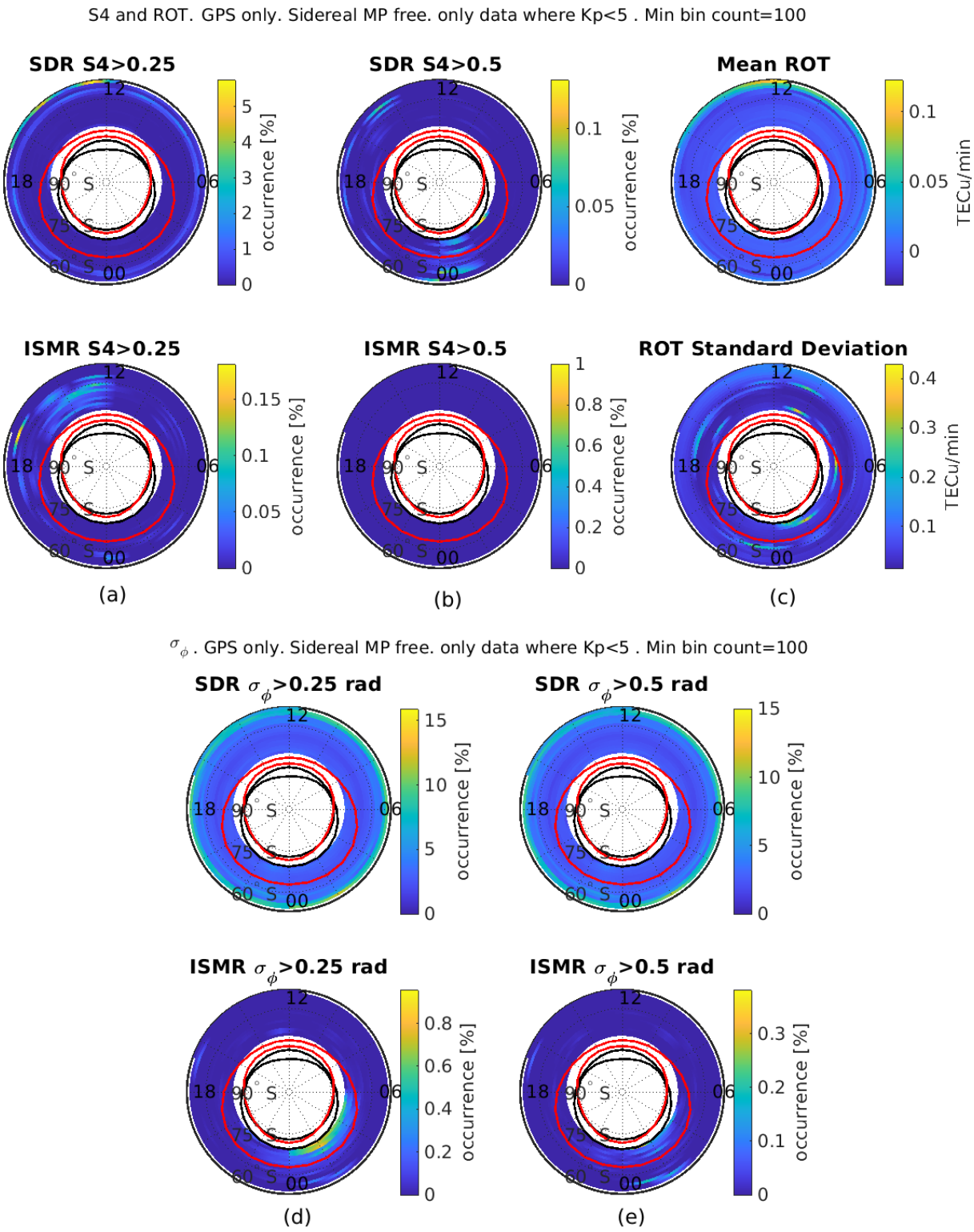

Figure 6. All the sidereal multipath free data from the two receivers when Kp < 5. (a-b) S4 from the SDR (top) and from the PolaRxS (bottom). (c) Mean (top) and standard deviation (bottom) of ROT. (d-e) σ_ϕ from the SDR (top) and PolaRxS (bottom).

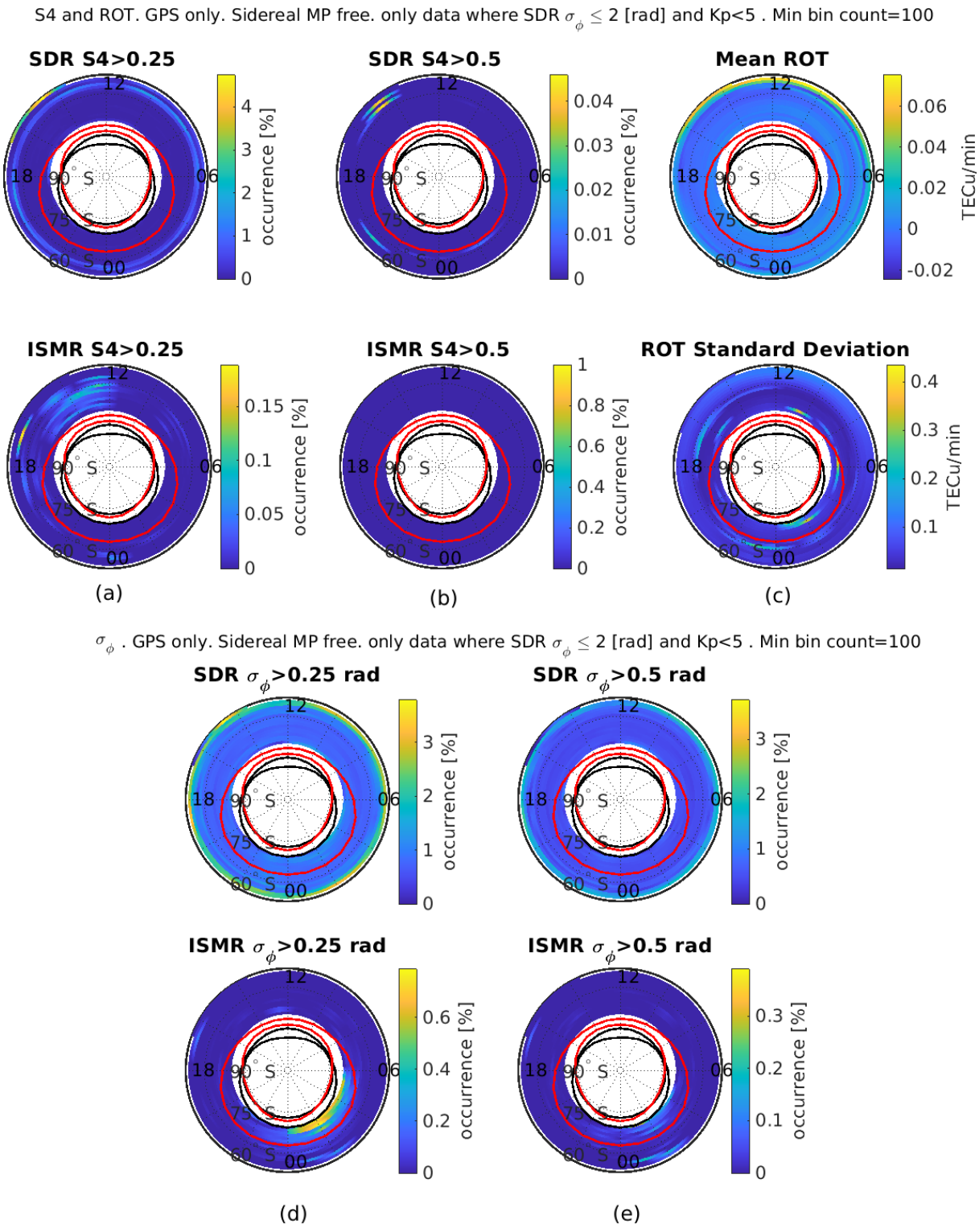

Figure 7. All the SDR phase scintillation anomaly-free data from the two receivers when Kp < 5. (a-b) S4 from the SDR (top) and from the PolaRxS (bottom). (c) Mean (top) and standard deviation (bottom) of ROT. (d-e) σ_ϕ from the SDR (top) and PolaRxS (bottom).

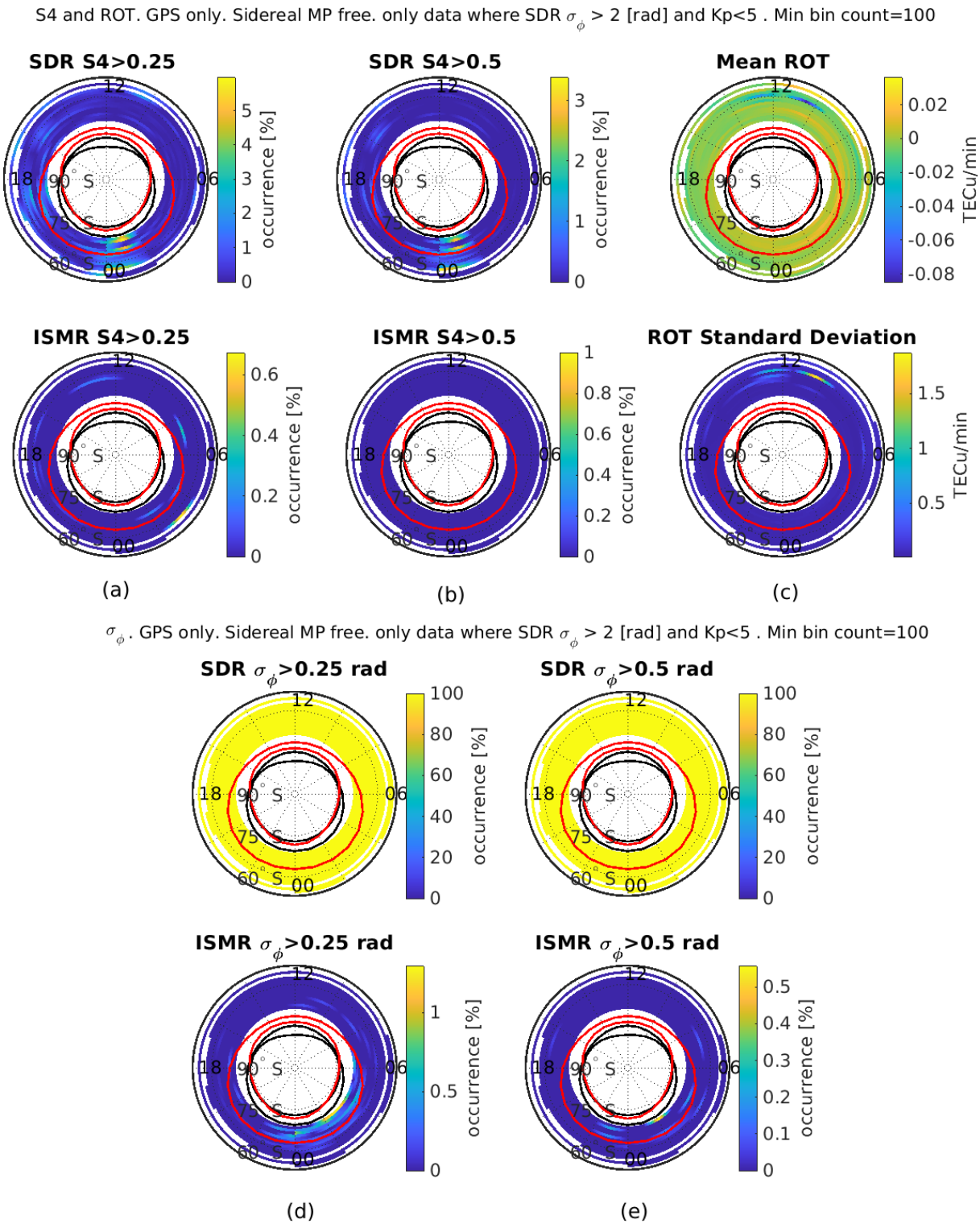

Figure 8. All the data with SDR phase scintillation anomaly from the two receivers when Kp < 5. (a-b) S4 from the SDR (top) and from the PolaRxS (bottom). (c) Mean (top) and standard deviation (bottom) of ROT. (d-e) σ_ϕ from the SDR (top) and PolaRxS (bottom).

4.2 $S4_{diff}$ and $\sigma_{\phi\ diff}$ under quiet conditions

Figure 9 shows the occurrence of the absolute differences in the indexes between the two receivers, $S4_{diff}$ (top) and $\sigma_{\phi\ diff}$ (bottom), under quiet conditions, when the difference (a) >0.25, and (b) >0.5. It also shows the (c) mean and (d) standard deviation of the index difference inside each bin.

$S4_{diff} > 0.25$ occurrence is dominant at the edge of IQ6 around 18:00 MLT while $S4_{diff} > 0.5$ is most noticeable at the edge of IQ0 AO between 02:00 and 04:00 MLT and at all MLATs between 00:00 and 02:00 MLT. The standard deviation of $S4_{diff}$ takes its biggest value outside the IQ6 AO at midnight MLT, and at the edge of the IQ6 AO right after midnight MLT. The fact that these differences' occurrences are aligned with the auroral oval suggests that the SDR might be informative for researchers studying ionospheric climate and weather.

On the other hand, the maps of $\sigma_{\phi\ diff}$ are not informative due to the high $\sigma_{\phi\ SDR}$ noise. Its occurrence above 0.5 rad exceeds 5% for all the bins, regardless of the magnetic coordinates, and has a higher occurrence towards the lower MLATs. The latter is attributed to the low C/N0 or even undetected multipath. Low C/N0 degrades the signal phase tracking, resulting in signal tracking noise.

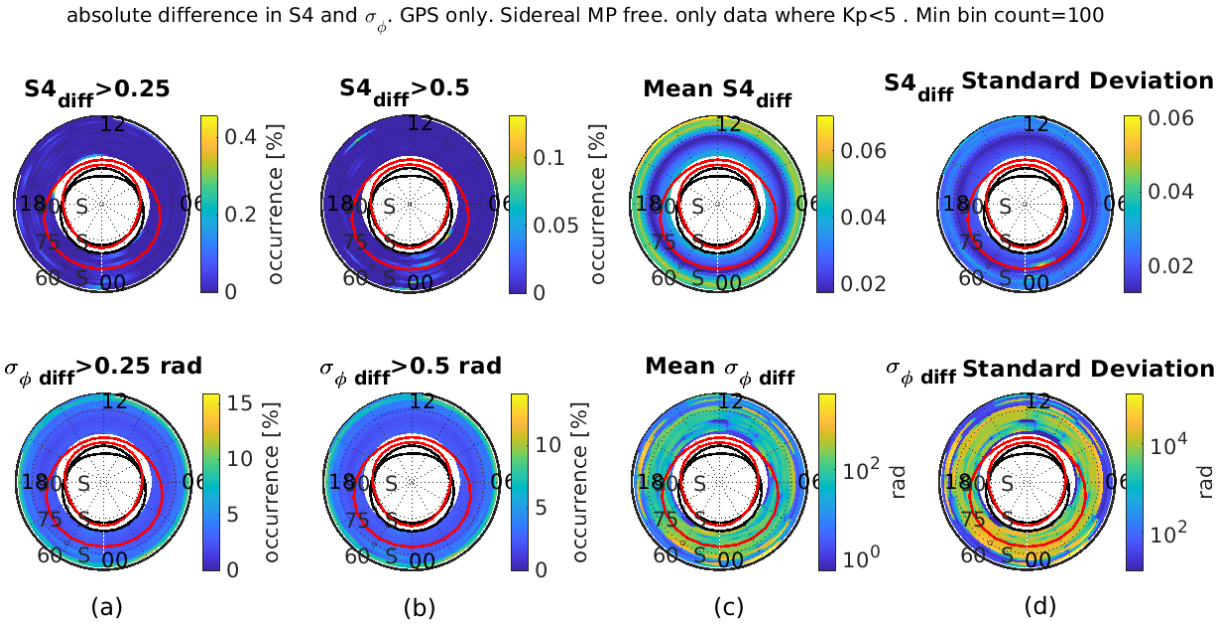

Figure 9. Climatology of the absolute difference in the S4 (top) and σ_ϕ (bottom) between the two receivers under quiet conditions (a) difference >0.25 (b) difference >0.5 (c) mean difference (d) standard deviation of the difference.

4.3 SDR vs. PolaRxS scintillation climatology under disturbed conditions

Figure 10 shows S4, σ_ϕ and ROT climatology maps under disturbed conditions (Kp ≥ 5) from the SDR (top) and PolaRxS (bottom) for (a) S4 > 0.25 (b) S4 > 0.5 (d) σ_ϕ > 0.25 rad (e) σ_ϕ > 0.5 rad (c) the mean (top) and standard deviation (bottom) of ROT.

Starting from the mean values of ROT, the highest positive ROT values can be observed at noon followed by negative ROT all afternoon. The standard deviation of ROT is high in the evening sector (19:00-23:00 MLT) exactly at the edge of IQ6 AO.

The SDR reveals strong amplitude scintillation S4 > 0.5 in the night sector (02:00-04:00 MLT) at the edge of IQ6 and in the morning sector at sub-auroral MLAT. The same scintillation occurrences are observed by PolaRxS but with S4 > 0.25. S4 > 0.5 is also observed but less frequently by the SDR at the edge of IQ6 in the evening sector (20:00-22:00 MLT). The latter could be due to multipath because it is separated by almost 12 hours MLT from the S4 occurrence in the morning sector. PolaRxS on the other hand did not observe any S4 > 0.5 under disturbed conditions.

The climatology of σ_ϕ from the two receivers are quite equivalent. Both receivers observe $\sigma_\phi > 0.25$ rad occurrence inside the IQ6 oval all night long (00:00-06:00 MLT) for both σ_ϕ thresholds: 0.25 and 0.5 rad. Indeed, the noise in SDR σ_ϕ is evident in its occurrence which is always above 2% at all MLATs and MLTs.

When the receivers are under disturbed conditions their respective climatology results are very similar in comparison with the quiet time when the SDR and PolaRxS maps result are significantly different. This result could be misinterpreted due to the small size of the disturbed conditions dataset. Nevertheless, our analysis demonstrates how the SDR performance is comparable to the PolaRxS under disturbed conditions (as shown in Figure 3).

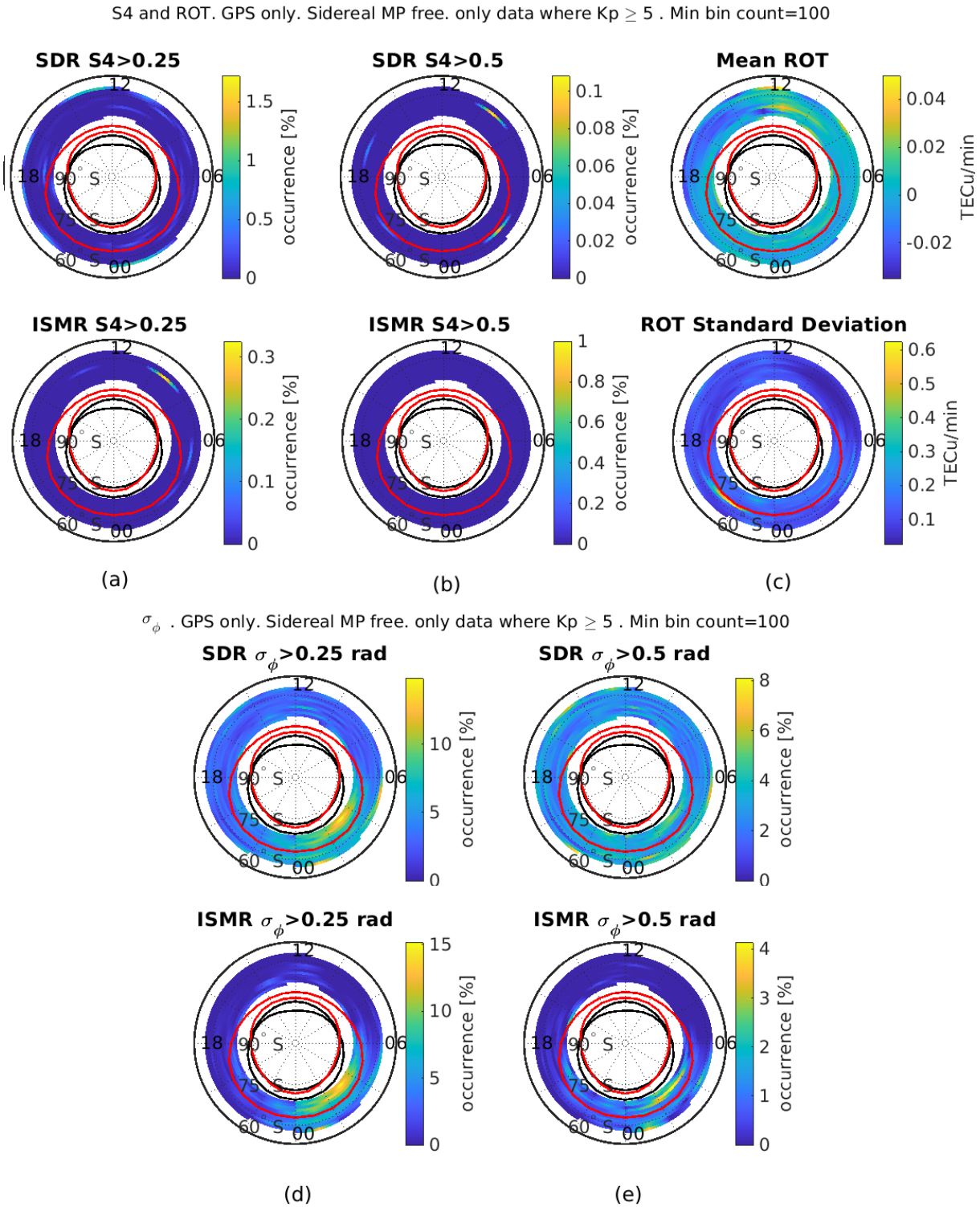

Figure 10. All the data from the two receivers when Kp ≥ 5. (a-b) S4 from the SDR (top) and from the PolaRxS (bottom), (c) Mean (top) and standard deviation (bottom) of ROT. (d-e) σ_ϕ from the SDR (top) and PolaRxS (bottom).

Figure 11 shows the climatology for the data where $\sigma_{\phi\ SDR} \leq 2$ rad under disturbed conditions. These maps are equivalent to the general case (Fig. 10) since this subset constitutes most of the dataset under disturbed conditions. No differences can be noticed neither in the mean and standard deviation of ROT maps nor in the σ_ϕ maps. For S4 maps, the occurrence of PolaRxS S4 > 0.25 and SDR S4 > 0.5 in the morning sector disappears, leaving the S4 occurrences at the edge of IQ6 AO night sector clearly visible.

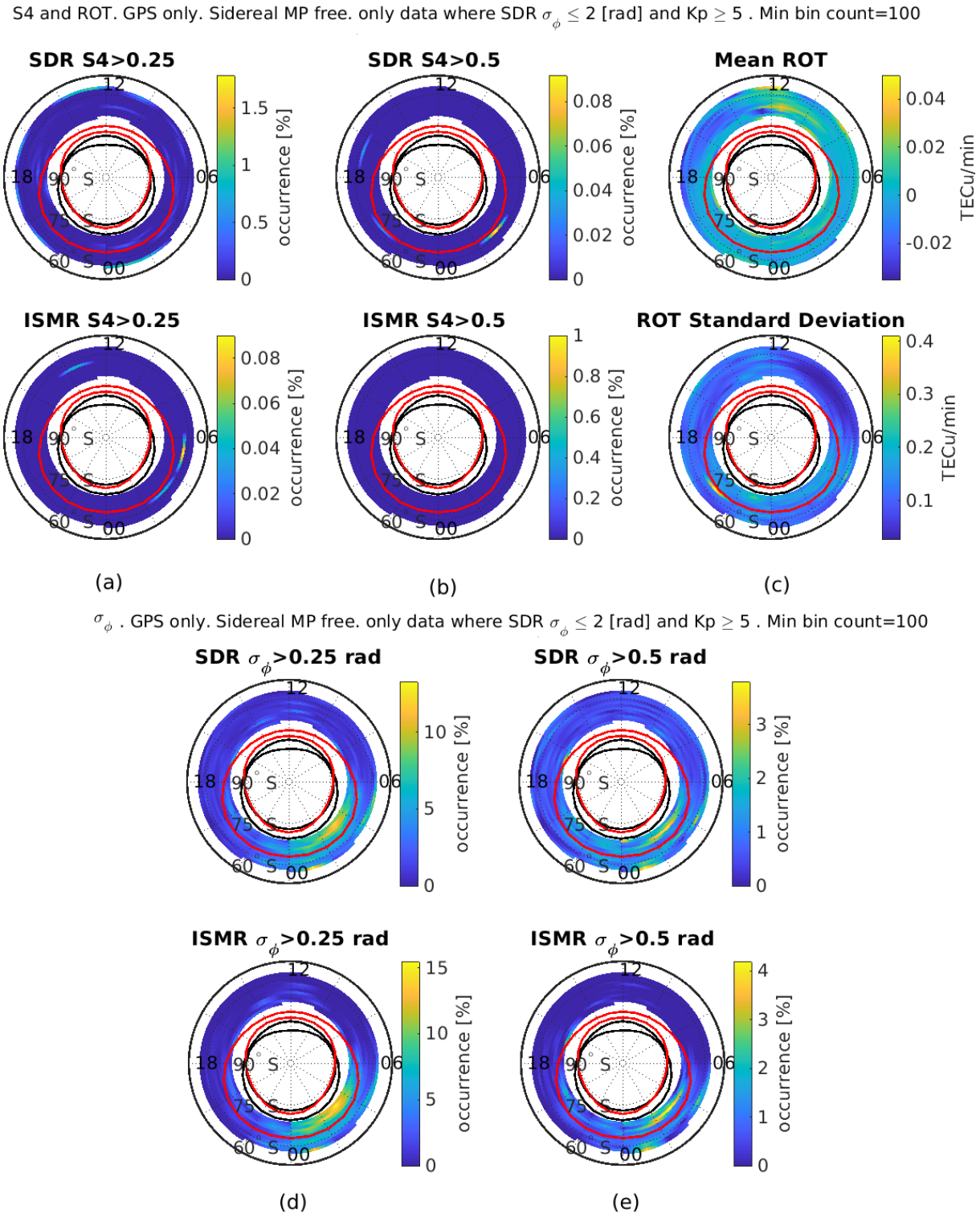

Figure 11. All the SDR phase scintillation anomaly-free data from the two receivers when Kp ≥ 5. (a-b) S4 from the SDR (top) and from the PolaRxS (bottom), (c) Mean (top) and standard deviation (bottom) of ROT. (d-e) σ_ϕ from the SDR (top) and PolaRxS (bottom).

Figure 12 shows a map representing all the data where the $\sigma_{\phi\ SDR}$ showed anomaly under disturbed conditions. The size of this subset of the dataset is so small that the minimum number of data points inside a bin was lowered to 1 sample/bin only. Thus, we do not call this figure a climatology, but rather a representation of the data. In this small subset of the data, both the mean and standard deviation of ROT maps have peak values at the edge of IQ6

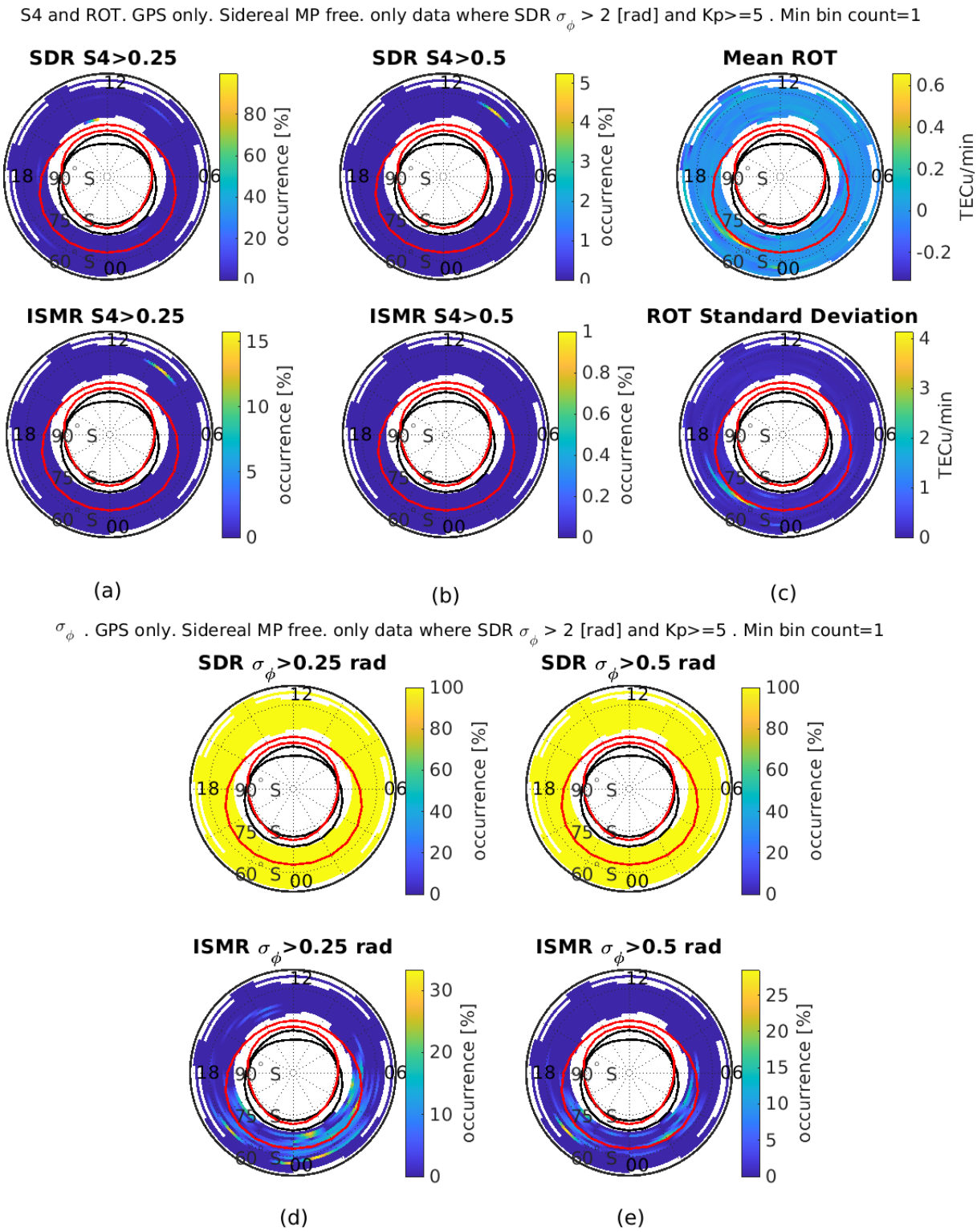

Figure 12. All the data with SDR phase scintillation anomaly from the two receivers when Kp ≥ 5. (a-b) S4 from the SDR (top) and from the PolaRxS (bottom), (c) Mean (top) and standard deviation (bottom) of ROT. (d-e) σ_ϕ from the SDR (top) and PolaRxS (bottom).

AO evening sector (18:00-23:00 MLT). Both receivers observed the occurrence of S4 > 0.25 in the morning sector at 60° S MLAT. The SDR observed in addition to that occurrence of S4 > 0.25 at the edge of IQ6 AO post-noon sector. σ_ϕ maps, although the ones from the SDR are useless, are interesting. Looking at PolaRxS $\sigma_\phi > 0.25$ rad, one can imagine the AO of this subset of data has expanded in all directions (i.e. MLTs) toward lower MLATs. Another oval can be imagined at 60°S MLAT spanning the evening and night sectors. $\sigma_\phi > 0.25$ rad maps also show clear occurrences of phase scintillation at the edge of IQ0 and IQ6 in the night sector. $\sigma_\phi > 0.5$ rad occurred at the edge of IQ6 at 02:00 MLT and at 60°S MLAT between 20:00-22:00 MLT.

4.4 $S4_{diff}$ and $\sigma_{\phi\ diff}$ under disturbed conditions

Figure 13 shows how the S4 index estimated by the two receivers under disturbed conditions differ by more than 0.25 at the outer edge of IQ6 around 18:00 and 04:00 MLT. $S4_{diff} > 0.5$ was not observed. The mean and standard deviation of $S4_{diff}$ have uniform occurrences for all MLTs, with higher values at the edges of the MLAT, suggesting differences in S4 computation due to the different receivers' noise variance as the C/N0 decreases.

$\sigma_{\phi\ diff}$ occurred mostly inside the IQ6 AO all evening and night sector, and outside the IQ6 oval towards low MLATs between 21:00-03:00 MLT. The mean and standard deviation of $\sigma_{\phi\ diff}$ reflect on SDR σ_ϕ peculiarities that are most noticeable at the edge of IQ6 AO 20:00-22:00 MLT and right after midnight, at the edge of IQ0 00:00-03:00 MLT, and in the morning and noon sector towards low MLATs. The fact that these differences are observed where irregularities formation are expected, further suggests that the SDR could be informative in scintillation data interpretation.

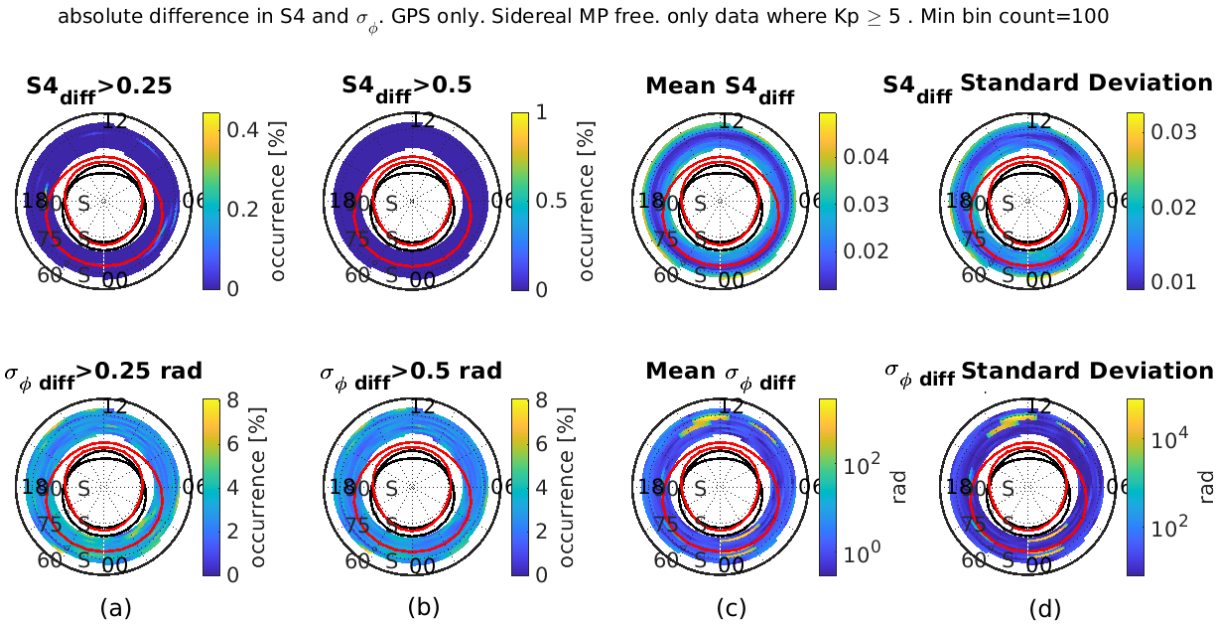

Figure 13. Climatology of the absolute difference in the S4 (top) and σ_ϕ (bottom) between the two receivers under disturbed conditions (a) difference >0.25 (b) difference >0.5 (c) mean difference (d) standard deviation of the difference.

4.5 Discussion and remarks

Table 1 shows a quantitative comparison between the absolute differences in S4 and σ_ϕ between the SDR and the PolaRxS receivers under quiet and disturbed conditions in terms of R_{diff}. The first column shows the parameter P, the second shows the threshold conditions on P_{SDR}, the third shows the geomagnetic conditions, the fourth shows the mean absolute difference in the index P from the two receivers $\langle |P_{SDR} - P| \rangle$, the fifth column is the average value of the index as estimated by PolaRxS $\langle P \rangle$, and the last column shows the computed R_{diff} according to Eq. (8).

As anticipated in the previous section, the normalized percentage difference seems to provide a non-negligible difference between the receivers. Just relying on Table 1, as was the case with Figure 6, we could say that the receivers are totally different tools. The mean values of the absolute differences in Table 1, and also in Fig. 9 and Fig. 13, are in alignment with values reported by [de Paula et al., 2021], where the differences in the scintillation indexes from 6 different receivers were analysed. In the latter study, approximately 4 days of data from low latitudes on scintillation days, were utilized, while in this article 4 years of high latitude data were utilised.

From R_{diff} reported in Table 1, the absolute average differences in the indexes from the two receivers under disturbed conditions are smaller compared to the quiet conditions. For example, the cases with $S4 > 0.5$ have R_{diff} approximately 1,400% under quiet condions and only 300% under disturbed conditions. The same is true for $0.5 < \sigma_\phi \leq 2$ that goes from approximately 3,200% under quiet conditions to only 223% under disturbed conditions. Indeed, these statistics could be biased and jeopardized by the small sample size of the data set under disturbed conditions w.r.t the data set under quiet conditions in the period 2016-2019 of low solar activity.

Nevertheless, the results observed in this table could help the investigation on using the SDR for space weather applications. The similarity between the climatological maps under disturbed conditions (Figures 10 and 12) suggests the ability of the SDR to work under strong scintillation conditions, however the high R_{diff} under quiet conditions hints that the SDR will be raising false alarms under quiet conditions and thus doubts the overall

Parameter (P)	Threshold β on SDR estimation	Geomagnetic condition	$\langle \lvert P_{SDR} - P \rvert \rangle$	$\langle P \rangle$	R_{diff}
S4	–	$Kp < 5$	0.024	0.052	47%
S4	$S4 > 0.25$	$Kp < 5$	0.25	0.103	244%
S4	$S4 > 0.5$	$Kp < 5$	0.799	0.057	1392%
S4	–	$Kp \geq 5$	0.019	0.052	36%
S4	$S4 > 0.25$	$Kp \geq 5$	0.212	0.105	202%
S4	$S4 > 0.5$	$Kp \geq 5$	0.404	0.135	300%
σ_ϕ	$\sigma_\phi \leq 2$ rad	$Kp < 5$	0.023	0.029	79%
σ_ϕ	$0.25 < \sigma_\phi \leq 2$ rad	$Kp < 5$	0.791	0.04	1941%
σ_ϕ	$0.5 < \sigma_\phi \leq 2$ rad	$Kp < 5$	1.053	0.03	3140%
σ_ϕ	$\sigma_\phi \leq 2$ rad	$Kp \geq 5$	0.025	0.054	46%
σ_ϕ	$0.25 < \sigma_\phi \leq 2$ rad	$Kp \geq 5$	0.356	0.31	115%
σ_ϕ	$0.5 < \sigma_\phi \leq 2$ rad	$Kp \geq 5$	0.757	0.34	223%
σ_ϕ	$\sigma_\phi > 2$ rad	$Kp < 5$	4713	0.03	15,875,509%
σ_ϕ	$\sigma_\phi > 2$ rad	$Kp \geq 5$	3077	0.08	3,892,803%

Table 1. Relative differences between climatological parameters derived from SDR and PolaRxS monitors.

proposal of SDR receivers for space weather monitoring. The fact that the disturbances under quiet conditions are not random and that they are focused at the edges of the auroral ovals (Figures 6 and 8) suggests further investigating these differences between the receivers. The receivers could have been tested and optimized to work well under disturbed conditions, resulting in inferior performance under quiet conditions. Also, the different post processing techniques implemented by the different receivers could be biased against effects that are dominant under quiet conditions, resulting in these noticeable differences under such conditions. These two assumptions could be addressed by further investigating the scintillation events identified by the SDR under quiet conditions using the high-rate data (50 Hz) available from both the SDR and PolaRxS receivers in this study. Furthermore, the IQ samples available from the SDR receiver under the quiet conditions could be re-processed using other receivers available from many research groups around the world, including the MATLAB-based SDR receiver developed by the NavSAS research group of Politecnico di Torino, where various parameters of the signal processing and post processing could be tuned.

Finally, under quiet geomagnetic condition, the ionosphere is not actually quiet [De Franceschi et al., 2019; Spogli et al., 2009] due to the many forces that affect the ionosphere, and thus those disturbances under quiet geomagnetic conditions identified by the SDR are worth investigation, and in this sense the SDR could play a role of an informative tool for ionospheric research community.

5. Conclusion

In this paper, we present a first look into the climatology of scintillation as observed from an SDR receiver under quiet and disturbed conditions. We process the longest SDR scintillation data collection, as far as we know. We show the climatology of S4 and σ_ϕ for two index thresholds: 0.25 and 0.5. We compare these climatology maps with the ones obtainable from a PolaRxS commercial ISM receiver sharing the same antenna with the SDR. We also show the climatology of the difference in S4 and σ_ϕ between the two receivers.

At first look, it seems that the climatology from the SDR under quiet conditions is significantly different from the commercial ISM receiver. However, carefully categorizing the data according to the occurrence of SDR phase measurement anomalies reveals that the SDR can be informative and can help researchers reveal interesting insights about ionospheric irregularities. In particular, the climatology of amplitude scintillation under quiet conditions from the SDR suggests a higher occurrence of S4 than the PolaRxS is reporting, especially at the edge of both the quiet and disturbed conditions auroral ovals in the night sector.

On the other hand, the climatology maps of S4 and σ_ϕ under disturbed conditions from both receivers are equivalent, except for the noise in the SDR σ_ϕ maps. This noise is uniformly present at all MLATs and MLTs and the real phase fluctuations occurrence is observed on top of the noise. Such performance for the SDR under challenging ionospheric conditions, confirms the ability of SDR receivers to process GNSS signals under scintillation conditions and suggests the feasibility of expanding the scope of the SDR from a tool used only for data recording and offline processing tool to a tool that can be used for operational space weather monitoring. The latter must be preceded by a careful inspection of the causes of the scintillation events detected by the SDR under quiet conditions in order to guarantee that the SDR would not be generating regular false alarms under quiet conditions.

The normalized percentage difference between the climatological parameters derived from the SDR and PolaRxS monitors under different geomagnetic conditions further confirms that on average, the differences between the two receivers indexes under disturbed conditions are smaller than the differences under quiet conditions. Indeed, these statistics could be biased and jeopardized by the fact that the number of samples under geomagnetic disturbed conditions are not as abundant as those under quiet conditions.

The SDR at SANAE IV stations has been running continuously for seven years. We showed the first results of the climatology from the SDR for the first four years, 2016-2019 that are quiet in terms of solar activity. The results encourage us to use the SDR as an informative tool for identifying and further analysing interesting scintillation and phase fluctuation events. In a future work, the spectral analysis for selected events both from the SDR and PolaRxS measurements is planned. Also, further processing for the SDR high-rate post-correlation measurements and the recording of the raw signal spectrum (I/Q samples) are foreseen. Finally, the results presented in this paper encourage us, and the scientific community who operate SDR receivers for scintillation monitoring, to keep operating the SDR system at SANAE and further develop it using the state-of-the-art SDR GNSS receivers for ionospheric scintillation.

Acknowledgement. The station at SANAE was deployed in the framework of the DemoGRAPE project funded by PNRA (Progetto di Ricerca 2013/C3.01) and it is run under the Memorandum of Understanding between INGV and SANSA (Delibera CdA INGV 297/2016).
The PolaRxS scintillation receiver's data are available from the eSWua website [Upper atmosphere physics and radiopropagation Working Group, 2020] (http://www.eswua.ingv.it/index.php/data-access-and-info/download-tool). https://doi.org/10.13127/ESWUA/GNSS.
Kp data are available from the website of the World Data Center for Geomagnetism, Kyoto (http://wdc.kugi.kyoto-u.ac.jp). The AACGM coordinates were calculated using the software package available from https://superdarn.thayer.dartmouth.edu/aacgm.html
Rayan Imam's current research fellowship is funded by the Swarm Space Weather Variability of Ionospheric Plasma (Swarm VIP) project, which has been funded by the European Space Agency, contract 4000130562/20/I-DT with the title "Swarm + 4D Ionosphere".
The Ph.D. work of I. Ebrahimi Mehr is supported by the grant DOT1332092 CUP E11B21006430005 funded within the Italian Programma Operativo Nazionale (PON) Ricerca e Innovazione 2014-2020, Asse IV "Istruzione e ricerca per il recupero" con riferimento all'Azione IV.4 "Dottorati e contratti di ricerca su tematiche dell'innovazione" e all'Azione IV.5 "Dottorati su tematiche green" DM 1061/2021.
A. Minetto acknowledges funding from the research contract no. 32-G-13427-5 DM 1062/2021 funded within the PON Ricerca e Innovazione of the Italian Ministry of University and Research.
The authors express their gratitude to Dr. Nicola Linty for his contribution to the deployment and the optimization of the station. The authors would like to thank Dr. Jayachandraan (University of New Bruswick) for his valuable suggestions regarding using the sidereal multipath mask.

References

Alfonsi, L., N. Bergeot, P.J. Cilliers, G. De Franceschi, L. Baddeley, E. Correia, D. Di Mauro, C. Enell, M. Engebretson, R. Ghoddousi-Fard, I. Häggström, Y. Bae Ham, G. Heygster, G. Jee, A. Kero, M. Kosch, H.J. Kwon, C. Lee, S. Lotz, … S. Zou (2022). Review of Environmental Monitoring by Means of Radio Waves in the Polar Regions: From Atmosphere to Geospace, Surv. Geophys, 43, 6, https://doi.org/10.1007/s10712-022-09734-z

Alfonsi, L., P.J. Cilliers, V. Romano, I. Hunstad, E. Correia, N. Linty, F. Dovis, O. Terzo, P. Ruiu, J. Ward and P. Riley, (2016). First Observations of GNSS Ionospheric Scintillations From DemoGRAPE Project, Space Weather, 14, 10, 704-709. https://doi.org/10.1002/2016SW001488

Alfonsi, L., L. Spogli, G. De Franceschi, V. Romano, M. Aquino, A. Dodson and C.N. Mitchell (2011). Bipolar climatology of GPS ionospheric scintillation at solar minimum, Radio Sci., 46, 3, https://doi.org/10.1029/2010RS004571

Baker, K.B. and S. Wing (1989). A new magnetic coordinate system for conjugate studies at high latitudes, J. Geophys. Res., 94, A7, https://doi.org/10.1029/ja094ia07p09139

Béniguel, Y. (2002). Global ionospheric propagation model (GIM): A propagation model for scintillations of transmitted signals. Radio Sci., 37, 3, 4-1-4-13. https://doi.org/10.1029/2000rs002393

Bougard, B., J.-M. Sleewaegen, L. Spogli, S.V. Veettil and J.F.G. Monico (2011). CIGALA: Challenging the Solar Maximum in Brazil with PolaRxS, 2572-2579, http://www.ion.org/publications/abstract.cfm?jp=p&articleID=9810

Briggs, B.H. and I.A. Parkin (1963). On the variation of radio star and satellite scintillations with zenith angle. J. Atmo. Terr. Phys., 25, 6, 339-366, https://doi.org/10.1016/0021-9169(63)90150-8

Chie Yeh, K. and C. Liu (1982). Radio Wave Scintillations in the Ionosphere Invited Paper, In PROCEEDINGS OF THE IEEE, 70, 4.

Cristodaro, C., F. Dovis, N. Linty and R. Romero (2018). Design of a Configurable Monitoring Station for Scintillations by Means of a GNSS Software Radio Receiver, IEEE Geosci. Remote Sens. Lett., 15, 3, 325-329, https://doi.org/10.1109/LGRS.2017.2778938

Cristodaro, C., L. Ruotsalainen and F. Dovis (2018). Benefits and limitations of the record and replay approach for GNSS receiver performance assessment in harsh scenarios, Sensors (Switzerland), 18, 7, https://doi.org/10.3390/s18072189

Crowley, G., G.S. Bust, A. Reynolds, I. Azeem, R. Wilder, B.W. O'Hanlon, M.L. Psiaki, S. Powell, T.E. Humphreyes and J.A. Bhatti (2011). CASES: A Novel Low-Cost Ground-based Dual-Frequency GPS Software Receiver and Space Weather Monitor, 1437-1446, http://www.ion.org/publications/abstract.cfm?jp=p&articleID=9702

Curran, J.T., M. Bavaro, A. Morrison and J. Fortuny (2014). Developing an Ionospheric Scintillation Monitoring Receiver. Inside GNSS, https://insidegnss.com/developing-an-ionospheric-scintillation-monitoring-receiver/

Curran, J.T., M. Bavaro, A. Morrison and J. Fortuny (2015). Operating a network of multi-frequency software-defined ionosphere monitoring receivers. 28th International Technical Meeting of the Satellite Division of the Institute of Navigation, ION GNSS, 2015, 5.

D'Angelo, G., M. Piersanti, A. Pignalberi, I. Coco, P. De Michelis, R. Tozzi, M. Pezzopane, L. Alfonsi, P. Cilliers and P. Ubertini (2021). Investigation of the physical processes involved in GNSS amplitude scintillations at high latitude: A case study, Remote Sensing, 13, 13, https://doi.org/10.3390/rs13132493

De Franceschi, G., L. Alfonsi, V. Romano, M. Aquino, A. Dodson, C.N. Mitchell, P. Spencer, A.W. Wernik (2008). Dynamics of high-latitude patches and associated small-scale irregularities during the October and November 2003 storms, J. Atmo. Solar-Terr. Phys., 70,6, https://doi.org/10.1016/j.jastp.2007.05.018

De Franceschi, G., L. Spogli, L. Alfonsi, V. Romano, C. Cesaroni and I. Hunstad (2019). the ionospheric irregularities climatology over svalbard from solar cycle 23, Sci. Rep., 9, 1, 9232, https://doi.org/10.1038/s41598-019-44829-5

de Paula, E.R., A.R.F. Martinon, A.O. Moraes, C. Carrano, A.C. Neto, P. Doherty, K. Groves, C.E. Valladares, G. Crowley, I. Azeem, A. Reynolds, D.M. Akos, T. Walter, T.L. Beach and J.-M. Slewaegen (2021). Performance of 6 Different Global Navigation Satellite System Receivers at Low Latitude Under Moderate and Strong Scintillation, Earth Space Sci., 8, 2, e2020EA001314. https://doi.org/10.1029/2020EA001314

Dovis, F., M. Pini, M. Spelat and P. Mulassano (2004). Benefits of a Reconfigurable Software GNSS Receiver in Multipath Environment, J. Global Pos. Sys., 3, 1 and 2, https://doi.org/10.5081/jgps.3.1.49

Feldshteyn, Y.I. (1963). On Morphology and Auroral and Magnetic Disturbances at High Latitudes, Geomagn. Aeron., 3, 183-192.

Fernandez, L., J.A. Ruiz-De-Azua, A. Calveras and A. Camps (2020). Assessing LoRa for satellite-to-earth communications considering the impact of ionospheric scintillation, IEEE Access, 8, https://doi.org/10.1109/ACCESS.2020.3022433

Fernández-Prades, C., L. Lo Presti and E. Falletti (2011). Satellite radiolocalization from GPS to GNSS and beyond: Novel technologies and applications for civil mass market, Proceedings of the IEEE, 99, 11, https://doi.org/10.1109/JPROC.2011.2158032

Forte, B. (2005). Optimum detrending of raw GPS data for scintillation measurements at auroral latitudes, J. Atmo. Solar-Terr. Phys., 67, 12 SPEC. ISS., 1100-1109, https://doi.org/10.1016/j.jastp.2005.01.011

Forte, B. and S.M. Radicella, (2002). Problems in data treatment for ionospheric scintillation measurements, Radio Sci, 37, 6, 8-1-8-5. https://doi.org/10.1029/2001rs002508

Fremouw, E.J., R.L. Leadabrand, R.C. Livingston, M.D. Cousins, C.L. Rino, B.C. Fair and R.A. Long (1978). Early results from the DNA Wideband satellite experiment-Complex-signal scintillation, Radio Sci., 13, 1, 167-187, https://doi.org/10.1029/RS013i001p00167

Ghobadi, H., C. Savas, L. Spogli, F. Dovis, A. Cicone and M. Cafaro (2020). A Comparative Study of Different Phase Detrending Algorithms for Scintillation Monitoring. 2020 33rd General Assembly and Scientific Symposium of the International Union of Radio Science, URSI GASS 2020, https://doi.org/10.23919/URSIGASS49373.2020.9232349

Ghobadi, H., L. Spogli, L. Alfonsi, C. Cesaroni, A. Cicone, N. Linty, V. Romano and M. Cafaro (2020). Disentangling ionospheric refraction and diffraction effects in GNSS raw phase through fast iterative filtering technique, GPS Solutions, 24,3, https://doi.org/10.1007/s10291-020-01001-1

Holmes, J.K. (1982). Coherent spread spectrum systems, R.E. Krieger Pub. Co.

Holzworth, R.H. and C.-I. Meng (1975). Mathematical representation of the auroral oval, Geophys. Res. Lett., 2, 9, https://doi.org/10.1029/GL002i009p00377

Hong, J., J.K. Chung, Y.H. Kim, J. Park, H.J. Kwon, J.H. Kim, J.M. Choix and Y.S. Kwak (2020). Characteristics of Ionospheric Irregularities Using GNSS Scintillation Indices Measured at Jang Bogo Station, Antarctica (74.62°S, 164.22°E), Space Weather, 18, 10, https://doi.org/10.1029/2020SW002536

Imam, R., L. Alfonsi, L. Spogli, C. Cesaroni and F. Dovis (2023). On estimating the phase scintillation index using TEC provided by ISM and IGS professional GNSS receivers and Machine Learning, Adv. Space Res., https://doi.org/10.1016/J.ASR.2023.07.039

Jin, Y., J.I. Moen, W.J. Miloch, L.B.N. Clausen and K. Oksavik (2016). Statistical study of the GNSS phase scintillation associated with two types of auroral blobs, J. Geophys. Res.: Space Phys., 121, 5, 4679-4697, https://doi.org/10.1002/2016JA022613

Kauristie, K., A. Morschhauser, N. Olsen, C.C. Finlay, R.L. McPherron, J.W. Gjerloev and H.J. Opgenoorth (2017). On the Usage of Geomagnetic Indices for Data Selection in Internal Field Modelling, In Space Sci. Rev., 206, 1-4, https://doi.org/10.1007/s11214-016-0301-0

Linty, N., F. Dovis, R. Romero, C. Cristodaro, L. Alfonsi and E. Correia (2016). Monitoring ionosphere over antarctica by means of a GNSS signal acquisition system and a software radio receiver, Institute of Navigation International Technical Meeting, ITM 2016, 2, https://doi.org/10.33012/2016.13433

Linty, N., A. Minetto, F. Dovis and L. Spogli (2018). Effects of phase scintillation on the GNSS positioning error during the September 2017 storm at Svalbard. Space Weather, 16(9), 1317-1329.

Linty, N., R. Romero, F. Dovis and L. Alfonsi (2015). Benefits of GNSS software receivers for ionospheric monitoring at high latitudes. 2015 1st URSI Atlantic Radio Science Conference, URSI AT-RASC 2015, https://doi.org/10.1109/URSI-AT-RASC.2015.7303110

Materassi, M., L. Alfonsi, G. De Franceschi, V. Romano, C. Mitchell and P. Spalla (2009). Detrend effect on the scalograms of GPS power scintillation, Adv. Space Res., 43, 11, 1740-1748, https://doi.org/10.1016/j.asr.2008.01.023

Materassi, M. and C.N. Mitchell (2007). Wavelet analysis of GPS amplitude scintillation: A case study, Radio Sci., 42, 1, https://doi.org/10.1029/2005RS003415

McCaffrey, A.M. and P.T. Jayachandran (2017). Spectral characteristics of auroral region scintillation using 100 Hz sampling, GPS Solutions, 21, 4, https://doi.org/10.1007/s10291-017-0664-z

McCaffrey, A.M. and P.T. Jayachandran (2019). Determination of the Refractive Contribution to GPS Phase "Scintillation.", J. Geophys. Res.: Space Physics, 124, 2, 1454-1469, https://doi.org/10.1029/2018JA025759

Mehr, I.E., A. Minetto, F. Dovis, E. Pica, C. Cesaroni and V. Romano (2023). An Open Architecture for Signal Monitoring and Recording Based on SDR and Docker Containers: A GNSS Use Case. IEEE EUROCON 2023 – 20th International Conference on Smart Technologies, 66-71, https://doi.org/10.1109/EUROCON56442.2023.10199078

Moen, J., K. Oksavik, L. Alfonsi, Y. Daabakk, V. Romano and L. Spogli (2013). Space weather challenges of the polar cap ionosphere, J. Space Weather Space Climate, 3, https://doi.org/10.1051/swsc/2013025

Morton, Y., H. Bourne, M. Carroll, Y. Jiao, N. Kassabian, S. Taylor, J. Wang, D. Xu and H. Yin (2014). Multi-constellation GNSS observations of equatorial ionospheric scintillation. 2014 31th URSI General Assembly and Scientific Symposium, URSI GASS 2014, https://doi.org/10.1109/URSIGASS.2014.6929773

Najmafshar, M. and S. Skone (2014). GNSS data processing investigations for characterizing ionospheric scintillation Polar Ionospheric Scintillation Model for GNSS View project, https://www.researchgate.net/publication/288760527

Nishimura, Y., T. Kelly, P.T. Jayachandran, S. Mrak, J.L. Semeter, E.F. Donovan, V. Angelopoulos and N. Nishitani (2023). Nightside High-Latitude Phase and Amplitude Scintillation During a Substorm Using 1-Second Scintillation Indices, J. Geophys. Res.: Space Phys., 128, 8, e2023JA031402, https://doi.org/10.1029/2023JA031402

Pica, E., A. Minetto, C. Cesaroni and F. Dovis (2023). Analysis and Characterization of an Unclassified RFI Affecting Ionospheric Amplitude Scintillation Index over the Mediterranean Area, IEEE J. Selected Top. Appl. Earth Obs. Remote Sensing, https://doi.org/10.1109/JSTARS.2023.3267003

Portella, I.P., A. de O Moraes, M. da Silva Pinho, J. Sousasantos and F. Rodrigues (2021). Examining the Tolerance of GNSS Receiver Phase Tracking Loop Under the Effects of Severe Ionospheric Scintillation Conditions Based on Its Bandwidth, Radio Sci., 56, 6, https://doi.org/10.1029/2020RS007160

Presti, L. Lo, P. Di Torino, E. Falletti, M. Nicola and M.T. Gamba (2014). Software Defined Radio technology for GNSS receivers, 2014 IEEE International Workshop on Metrology for Aerospace, MetroAeroSpace 2014 – Proceedings, https://doi.org/10.1109/MetroAeroSpace.2014.6865941

Priyadarshi, S. (2015). A Review of Ionospheric Scintillation Models. In Surveys in Geophysics (Vol. 36, Issue 2). https://doi.org/10.1007/s10712-015-9319-1

Rino, C.L., M.D. Cousins and J.A. Klobuchar (1981). Amplitude and phase scintillation measurements using the Global Positioning System, In: Symposium on the Effect of the Ionosphere on Radiowave Systems.

Secan, J.A., R.M. Bussey, E.J. Fremouw and S. Basu (1997). High-latitude upgrade to the Wideband ionospheric scintillation model, Radio Sci., 32, 4, 1567-1574, https://doi.org/10.1029/97RS00453

Shepherd, S.G. (2014). Altitude-adjusted corrected geomagnetic coordinates: Definition and functional approximations, J. Geophys. Res.: Space Physics, 119, 9, https://doi.org/10.1002/2014JA020264

Spogli, L., L. Alfonsi, G. De Franceschi, V. Romano, M.H.O. Aquino and A. Dodson (2009). Climatology of GPS ionospheric scintillations over high and mid-latitude European regions, Annales Geophysicae, 27, 9, 3429-3437, https://doi.org/10.5194/ANGEO-27-3429-2009

Spogli, L., H. Ghobadi, A. Cicone, L. Alfonsi, C. Cesaroni, N. Linty, V. Romano and M. Cafaro (2022). Adaptive Phase Detrending for GNSS Scintillation Detection: A Case Study over Antarctica, IEEE Geosci. Remote Sensing Lett., 19, https://doi.org/10.1109/LGRS.2021.3067727

Spogli, L., D. Sabbagh, M. Regi, C. Cesaroni, L. Perrone, L. Alfonsi, D. Di Mauro, S. Lepidi, S.A. Campuzano, D. Marchetti, A. De Santis, A. Malagnini, C. Scotto, G. Cianchini, X.H. Shen, A. Piscini and A. Ippolito (2021). Ionospheric Response Over Brazil to the August 2018 Geomagnetic Storm as Probed by CSES-01 and Swarm Satellites and by Local Ground-Based Observations, J. Geophys. Res.: Space Phys., 126, 2, https://doi.org/10.1029/2020JA028368

Ulversoy, T. (2010). Software defined radio: Challenges and opportunities, IEEE Communications Surveys and Tutorials, 12, 4, https://doi.org/10.1109/SURV.2010.032910.00019

Upper atmosphere physics and radiopropagation Working Group. (2020). Electronic Space Weather upper atmosphere database (eSWua) – GNSS scintillation data (1.0), Istituto Nazionale di Geofisica e Vulcanologia (INGV), https://doi.org/10.13127/eswua/gnss

Van Dierendonck, A.J. and B. Arbesser-Rastburg (2004). Measuring Ionospheric Scintillation in the Equatorial Region Over Africa, Including Measurements From SBAS Geostationary Satellite Signals. Proceedings of the 17th International Technical Meeting of the Satellite Division of The Institute of Navigation (ION GNSS 2004), 316-324.

Van Dierendonck, A.J., J. Klobuchar and Q. Hua (1993). Ionospheric scintillation monitoring using commercial single frequency C/A code receivers, Proceedings of ION GPS, 93, 1333-1342.

Wang, Y., Q.H. Zhang, P.T. Jayachandran, J. Moen, Z.Y. Xing, R. Chadwick, Y.Z. Ma, J.M. Ruohoniemi and M. Lester (2018). Experimental Evidence on the Dependence of the Standard GPS Phase Scintillation Index on the Ionospheric Plasma Drift Around Noon Sector of the Polar Ionosphere, J. Geophys. Res. Space Phys., 123, 3, https://doi.org/10.1002/2017JA024805

Wernik, A.W., L. Alfonsi and M. Materassi (2007). Scintillation modeling using in situ data. Radio Science, 42, 1, n/a-n/a, https://doi.org/10.1029/2006rs003512

Zhang, J., I.G. Richardson, D.F. Webb, N. Gopalswamy, E. Hutrunen, J.C. Kasper, N.V. Nitta, W. Poomvises, B.J. Thompson, C.C. Wu, S. Yashiro and A.N. Zhukov (2007). Solar and interplanetary sources of major geomagnetic storms (Dst ≤ −100 nT) during 1996-2005, J. Geophys. Res. Space Phys., 112, 10, https://doi.org/10.1029/2007JA012321

***CORRESPONDING AUTHOR: Rayan IMAM**,
Upper Atmosphere Physics and Radiopropagation Unit, Istituto Nazionale di Geofisica e Vulcanologia, Rome, Italy
e-mail: rayan.imam@ingv.it